Colloids and Surfaces B: Biointerfaces 270 (2027) 116258

Contents lists available at ScienceDirect

Colloids and Surfaces B: Biointerfaces

journal homepage: www.elsevier.com/locate/colsurfb

GM1 oligosaccharide reprograms Neuro2a-derived extracellular vesicles for selective, low-disruption membrane interactions

Sally Helmy [a,b,1], Giulia Lunghi [a], Alexandros Koutsioubas [c], Stephen C.L. Hall [d], Miriam Grava [a,e], Hendrik Vondracek [f,g,2], László Almásy [h], László Bottyán [h,m], Martin Rosenthal [i], Maria Fazzari [a], Laura Mauri [a], Maria Grazia Ciampa [a], Chiara Adriana Elia [j,k], Elena Monica Borroni [a,k], Sandro Sonnino [a], Pietro Parisse [f,l], Paola Brocca [a], Elena Chiricozzi [a,*], Loredana Casalis [f,*], Valeria Rondelli [a,*]

[a] Department of Medical Biotechnology and Translational Medicine, Università Degli Studi di Milano, Milano, Italy
[b] Biophysics Group, Physics Department, Faculty of Science, Ain Shams University, Cairo, Egypt
[c] Julich Centre for Neutron Science (JCNS) at Heinz Maier-Leibnitz Zentrum (MLZ), Forschungszentrum Julich GmbH, Garching, Germany
[d] ISIS Neutron and Muon Source, Rutherford Appleton Laboratory, Didcot, OX11 0DE, UK
[e] Institute for Condensed Matter Physics, TU Darmstadt, Hochschulstraße 8, Darmstadt, 64289, Germany
[f] ElettraSincrotrone Trieste, Strada Statale 14 km 163.5 in Area Science Park Basovizza, Trieste, 34149, Italy
[g] Diamond Light Source, Harwell Science and Innovation Campus, Chilton, Didcot, OX11 0DE, UK
[h] Budapest Neutron Centre, HUN-REN Centre for Energy Research, Budapest, 1121, Hungary
[i] Department of Chemistry, KU Leuven, Celestijnenlaan 200f, Leuven, 3001, Belgium
[j] Institute of Neuroscience (IN-CNR), Consiglio Nazionale delle Ricerche, Milan, Italy
[k] RCCSHumanitas Research Hospital, via Manzoni 56, Milan, Rozzano, 20089, Italy
[l] CNR - IOM, Basovizza, TS, Italy
[m] HUN-REN Wigner Research Centre for Physics, Department of Nuclear Materials Science, Budapest, Hungary

ARTICLE INFO

Keywords:
GM1 ganglioside
GM1 oligosaccharide
Extracellular Vesicles
Small angle scattering
Atomic force microscopy
Lipid model membranes
Differential scanning calorimetry
Neutron reflectometry
Fourier-transform infrared spectroscopy
Neurodegenerative diseases

ABSTRACT

The GM1 oligosaccharide β-Gal-(1−3)-β-GalNAc-(1−4)-[α-Neu5Ac-(2−3)]-β-Gal-(1−4)-Glc (OligoGM1) represents the soluble, bioactive portion of GM1 ganglioside and recapitulates many of its trophic, protective, and restorative effects. Our previous proteomic studies on OligoGM1-treated neuroblastoma cells revealed alterations in endocytic trafficking and extracellular vesicles (EVs) biogenesis suggesting a potential role for OligoGM1 in modulating EV biogenesis. Here, we apply a multi-technique biophysical platform to investigate the physicochemical properties and functionality of EVs released by murine neuroblastoma Neuro2a cells, treated with OligoGM1. We show that OligoGM1 treatment slightly shifts to lower values the EVs' size population distribution and increases their relative lipid content, accompanied by a higher proportion of membrane-associated proteins. Our analysis further indicates that OligoGM1-treated cells release EVs with altered bilayer structural parameters, including increased apparent membrane thickness, consistent with a modified distribution of lipid/protein contributions within the adopted membrane model. Functional characterization using biomimetic model membranes indicates that EVs from treated and untreated cells differ in protein insertion and lipid exchange efficiency, pointing to distinct membrane-interaction modes relevant to downstream cellular interactions. Overall, these findings suggest that OligoGM1 reshapes the molecular architecture and biophysical behaviour of Neuro2a-derived EVs, providing membrane-level fingerprints that may be relevant for future studies of EV–cell interactions in neurodegenerative models.

* Corresponding authors.
E-mail address: valeria.rondelli@unimi.it (V. Rondelli).
[1] Present address: Biophysics Group, Physics Department, Faculty of Science, Ain Shams University, Cairo, Egypt.
[2] Present address: Diamond Light Source, Harwell Science and Innovation Campus, Chilton - Didcot, OX11 0DE, Oxfordshire, UK

https://doi.org/10.1016/j.colsurfb.2026.116258
Received 6 July 2026; Received in revised form 21 September 2026; Accepted 13 October 2026
Available online 14 October 2026
0927-7765/© 2026 The Author(s). Published by Elsevier B.V. This is an open access article under the CC BY license (http://creativecommons.org/licenses/by/4.0/).

1. Introduction

Extracellular vesicles (EVs) are lipid bilayer-enclosed nanostructures secreted by virtually all cell types and detected in most biological fluids [1,2]. Including exosomes and microvesicles, EVs closely mirror the molecular composition of their cells of origin [3] and transport biologically active cargo (i.e. lipids, proteins, and nucleic acids) that mediates intercellular communication in both physiological and pathological contexts. Accordingly, EVs are increasingly recognized as key biological effectors and as promising therapeutic tools [4], contributing to tissue homeostasis as well as to disease modulation, in conditions such as cancer, cardiovascular disorders, or neurodegeneration [5–7].

EV function is intrinsically governed by their molecular architecture and complex physico-chemical landscape, which encompass variations in size, lipid composition, membrane fluidity, surface charge, and the dynamic biomolecular corona [8,9]. These structural and biophysical traits define how EVs engage with recipient cell membranes and navigate intracellular trafficking pathways [9]. EV-mediated signalling and cargo transfer depend on interfacial coupling events that range from receptor-mediated docking and endocytic internalization to membrane-membrane merging [9,10]. From a biophysical standpoint, membrane fusion is a tightly regulated multi-step process—progressing from initial hydration/dehydration barriers to stalk formation, hemifusion diaphragm expansion, and fusion pore opening—governed by lipid curvature stress, lateral phase separation, and line tension at domain boundaries [10].

Despite recent advances in live-cell tracking and single-particle characterization [11,12], unravelling how specific compositional modifications during EV biogenesis translate into distinct membrane-level interaction regimes remains a central challenge [8,10,13]. Dissecting these nanoscale coupling mechanisms using controlled biomimetic membranes provides essential, component-resolved insight into EV interfacial behavior upstream of cellular uptake [8–10,14,15–19].

Gangliosides, and particularly GM1, are emerging as key molecular determinants at the interface between membrane organization, signalling, and vesicular trafficking in neurons. GM1 is a major neuronal ganglioside highly enriched in the plasma membrane [20] where it contributes, together with other glycosphingolipids, to the formation of lipid rafts, specialized microdomains that regulate synaptic curvature, electrical properties, and receptor compartmentalization. These domains play essential roles in synaptic integrity, signal transduction, and neural homeostasis [21]. Notably, many receptors localized in lipid rafts, including neurotrophin Trk receptors, critically depend on GM1 for optimal signalling. GM1 enhances Trk activation and downstream pathways involved in neuroprotection, calcium signalling, and mitochondrial function [22–27].

Importantly, it has been shown that the GM1 oligosaccharide (OligoGM1), a pentasaccharide composed of four neutral sugars and one negatively charged sialic acid (Fig. 1), stabilizes the TrkA–NGF complex, enhances receptor signalling, and activates downstream pathways involved in neuronal survival, calcium homeostasis, mitochondrial function, and protection against excitotoxicity.

Furthermore, its small size and water solubility enable OligoGM1 to cross the blood-brain barrier (BBB), making it a particularly attractive therapeutic candidate for central neurodegenerative disorders [20, 29–31].

Although research specifically focused on the isolated GM1 oligosaccharide remains limited, a recent study by an independent group provided additional evidence for the biological activity of OligoGM1 in a related experimental model [32]. This independent observation supports the broader relevance of OligoGM1-mediated effects beyond the experimental systems investigated by our group.

Importantly, previous molecular and proteomic analyses of OligoGM1-treated Neuro2a (N2a) cells showed that this neurotrophic signalling response is accompanied by broader changes in cellular pathways. In particular, OligoGM1 treatment altered the expression of proteins involved in endosomal and endocytic trafficking, including proteins associated with multivesicular-body dynamics, EV biogenesis, secretion, and targeting (Table S1). These proteins include Rab3a, Rab10, VPS28, and other regulators of vesicular trafficking. This molecular profile suggested that the effects of OligoGM1 may extend beyond the intracellular signalling response and influence the properties of the EVs released by treated cells.

This observation provided the rationale for the present study. We asked whether OligoGM1-induced changes in the parental cells are reflected in the composition and membrane architecture of their EVs and whether these EVs consequently display different interactions with model membranes. This question cannot be addressed through measurements of EV concentration and size alone, because treatment-dependent changes in lipid–protein organization may occur without substantial alterations in these bulk parameters. We therefore combined conventional EV characterization with complementary membrane-sensitive biophysical techniques to compare the composition, bilayer structure, membrane remodelling, lipid exchange, and incorporation of EV-derived material for Ctrl- and OligoGM1-EVs [33–35].

To the best of our knowledge, this is the first study to characterize the membrane architecture and interfacial behaviour of EVs released by OligoGM1-treated cells.

Accordingly, within this N2a model, we hypothesize that OligoGM1-driven modulation of cellular trafficking/biogenesis yields EVs with altered lipid–protein architecture and bilayer structure, which biases EV–membrane interactions toward distinct regimes. The specific aims are to determine whether EVs derived from treated versus untreated cells differ in (i) nanoscale membrane features (spectroscopic protein/

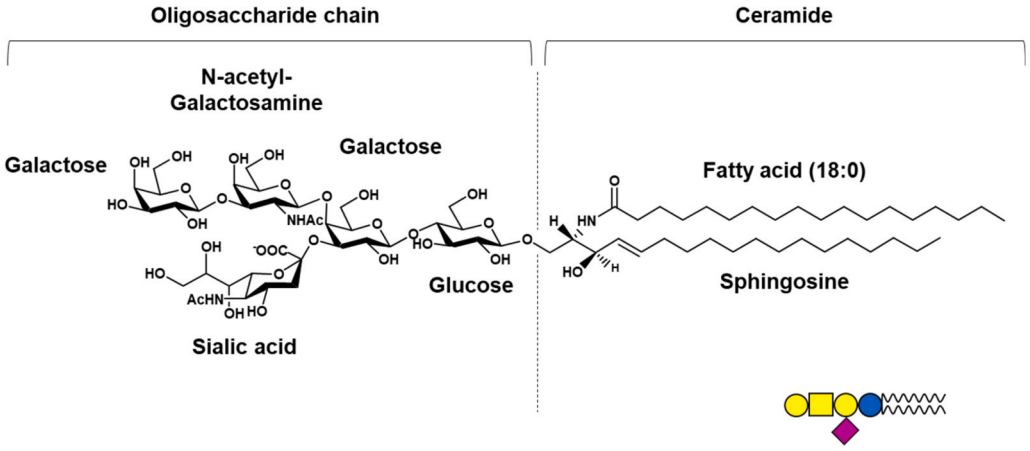


Fig. 1. Structure of Ganglioside GM1. Oligosaccharide sugar geometric and colour code is according to Varki et al. [28].

lipid balance and scattering-derived bilayer parameters) and (ii) functional interfacial readouts that are relevant upstream of cellular uptake, including domain-selective docking on raft-like bilayers, lipid exchange dynamics, and depth-resolved incorporation of EV-derived material into model membranes [13].

The study does not establish a direct causal link between individual signalling proteins and specific EV properties; rather, it tests whether the previously reported OligoGM1-induced cellular changes are accompanied by measurable structural and interaction fingerprints in the released EVs.

2. Materials and methods

2.1. Materials

Commercial chemicals were of the highest purity available, common solvents were distilled before use, and the milliQ water was doubly distilled in a glass apparatus.

Cell culture plates were obtained from Corning (Corning, NY, USA). Mouse neuroblastoma N2a cells (RRID: CVCL_0470), phosphate-buffered saline (PBS), bovine serum albumin (BSA), free fatty acids–BSA, trypan blue, ethylenediaminetetraacetic acid, dimethyl sulfoxide, sodium orthovanadate, Tween-20, 1,4-dithiothreitol (DTT), bromophenol blue, glycerol, glucose, the primary polyclonal rabbit anti-TSG101 (RRID: AB_609889), high-performance thin-layer chromatography (HPTLC), Triton X-100 and the primary polyclonal rabbit anti-TSG101 antibody (RRID:AB_609889) were obtained from Merck Millipore (Darmstadt, Germany).

Non-fat dry milk was purchased from Regilait (Saint-Martin-Belle-Roche, France). Dulbecco's modified Eagle's (DMEM) high-glucose medium, foetal bovine serum (FBS), L-glutamine, sodium pyruvate, and penicillin and streptomycin (P/S, penicillin 10,000 U/mL and streptomycin 10 mg/mL) solution were obtained from EuroClone (Paignton, UK). The primary monoclonal mouse anti-calnexin antibody (RRID:AB_397884) was obtained from BD Bioscience (Heidelberg, Germany). The primary monoclonal rabbit anti-Alix antibody (RRID: AB_2800192), the primary monoclonal rabbit anti-CD9 antibody (RRID: AB_2732848), and the secondary goat-anti-rabbit HRP-conjugated antibody (RRID:AB_2099233) were obtained from Cell Signalling Technology (Danvers, MA, USA). The secondary goat-anti-mouse HRP conjugated antibody (RRID:AB_228307) was obtained from Thermo Fisher Scientific (Waltham, MA, USA).

2.2. OligoGM1 preparation

OligoGM1 was prepared by ozonolysis from GM1 followed by alkaline degradation as previously described [36–38]. GM1 ganglioside was purified from the total ganglioside mixture extracted from fresh pig brains collected at the slaughterhouse of the Galbani Company (Melzo, Italy) [39]. The ganglioside mixture, 5 g sialic acid, was dissolved in pre-warmed (36 °C) 500 mL of 0.05 M sodium acetate, 1 mM $CaCl_2$ buffer (pH = 5.5). *Vibrio cholerae* sialidase (1 unit) was added to the solution every 12 h to transform the major part of polysialogangliosides into GM1 and obtain higher amount of GM1 [40]. Incubation at 36 °C was maintained for two days with magnetic stirring, and the solution dialyzed at 23 °C for 4 days against 10 L of water changed 5 times a day. The sialidase treated ganglioside mixture was subjected to 150 cm x 2 cm silica gel 100 column chromatography equilibrated and eluted with chloroform/methanol/water (60:35:5 v/v/V). The fractions containing GM1, identified by High Performance Thin-Layer Chromatography (HPTLC), were pooled, dried and submitted to a further column chromatographic purification using the above experimental conditions. Fractions containing pure GM1 were collected and dried. The residue was dissolved in chloroform/methanol (2:1 v/v) and precipitated by adding 4 volumes of cold acetone. After centrifugation (at 15,000 *x* g), the GM1 pellet was separated from the acetone, dried, dissolved in 50 mL of deionized water and lyophilized, yielding 1.35 g of white powder which was stored at −20 °C.

To obtain OligoGM1, GM1 was dissolved in methanol and slowly saturated with ozone at 23 °C. The solvent was then evaporated under vacuum and the residue brought immediately to pH = 10.5–11.0 by addition of triethylamine (TEA). After 3 days, the TEA solution was evaporated and OligoGM1 was purified by flash chromatography using chloroform/methanol/2-propanol/water (60:35:5:5 v/v/v) as eluent. The oligosaccharide was dissolved in methanol and stored at 4 °C. By nuclear magnetic resonance, mass spectrometry, and HPTLC analyses, the homogeneity of OligoGM1 was verified to be over 99% [41].

2.3. N2a cell cultures

Wild-type (WT) murine N2a cells were maintained as a monolayer in DMEM high glucose medium supplemented with 10% heat inactivated FBS (56 °C for 30 min), 1% L-glutamine, 1% P/S and 1 mM sodium pyruvate, at 37 °C in a 95% air/ 5% CO_2 atmosphere. Cells were subcultured to a fresh culture when confluence of 80–90% was reached (i.e. every 3–4 days).

2.4. Cell treatments

N2a cells were seeded at 15×10^3 cells/cm^2 and incubated for 48 h to allow cells attachment and recovery in complete medium before treatments. To study the OligoGM1 effect, growth medium was removed and N2a cells were pre-incubated in pre-warmed (37 °C) DMEM high-glucose FBS-free medium containing 1% L-glutamine, 1% P/S and 1 mM sodium pyruvate for 30 min at 37 °C. Cell treatments were performed in FBS free culture medium in order to reduce the serum contaminants (i.e. lipoproteins). Sequentially, cells were incubated at 37 °C for 24 h in the presence of 50 μM OligoGM1, condition that was previously found to promote neurodifferentiation and neuroprotection in N2a cells via the activation of the TrkA-ERK1/2 signalling pathway [33,42,43] cells were incubated under the same experimental conditions but omitting any addition of OligoGM1.

2.5. Isolation of EVs

The EVs were isolated by ultracentrifugation according to the protocols described in [14]. Briefly, cell medium was collected and centrifuged (300 *x* g) for 10 min at 4 °C to clarify cell-conditioned medium. The clarified cell conditioned medium was filtered through 0.2 μm PES filters for removing the large EVs, free circulating lipoproteins and other contaminants. The eluted medium was concentrated using Amicon Ultra 4 centrifuge filters (30 kDa, Millipore-Sigma, Burlington, MA, USA) and centrifuged (3300 *x* g) for 1 h at 4 °C. The supernatant was collected into polypropylene centrifuge tubes and ultracentrifuged (120,000 *x* g) for 1 h at 4 °C. The final pellet containing the EVs was resuspended in PBS, then aliquoted and stored at −80 °C until analysis. EVs isolated from the OligoGM1 treated cells were then identified as (OligoGM1-EVs), while those isolated from the untreated control cells were identified as (Ctrl-EVs). Differential ultracentrifugation combined with filtration enriches EV-containing fractions but does not yield molecularly pure EV preparations; co-isolation of soluble proteins, protein aggregates, lipoproteins, or other extracellular biomolecular components cannot be fully excluded [44]. Since Ctrl- and OligoGM1-EVs were isolated using the same workflow, the present study provides a controlled comparative analysis between the two conditions. From a biointerface perspective, the resulting EV-enriched preparations are considered biologically relevant soft nanocolloidal entities, whose interfacial behaviour may include contributions from associated biomolecular components or an effective corona.

2.6. Protein analysis

To ensure the specificity and purity of the isolated small EVs, immunoblotting analysis was performed on purified EVs and N2a cell lysate. Briefly, N2a cells grown in the presence or in the absence of OligoGM1 were washed twice with PBS containing 1 mM sodium orthovanadate, lysed using hot (90 °C) Laemmli buffer 1.5 x (0.15 M DTT, 94 mM Tris-HCl pH 6.8, 15% glycerol, 3% w/v SDS, 0.015% w/v bromophenol blue) and sonicated with Vibra-cellTM (Sonics & Materials, Inc. Danbury, CT, USA) for 3 times (10 s at 25–30 amplitude). In the same manner, EVs resuspended in PBS were mixed with Laemmli buffer. Aliquots from cell lysate and EVs were boiled (95 °C, 5 min) and proteins were separated on a 4–20% precast gel and transferred to PVDF membranes using the Trans-Blot® Turbo™ Transfer System (Bio-Rad) with the mixed molecular weight protocol for 7 min. After protein transfer, PVDF membranes were incubated for 1 h in blocking solution [Tris-buffered saline containing 0.1% Tween-20 (TBS-T) and 5% non-fat dry milk] at 23 °C and then incubated for 16 h at 4 °C with primary antibodies at the proper dilution: polyclonal rabbit anti-TSG101 (1:1000 in 5% milk in TBS-T), monoclonal mouse anti-calnexin (1:1000 in 5% BSA in TBS-T), monoclonal rabbit anti-Alix (1:1000 in 5% milk in TBS-T), monoclonal rabbit anti-CD9 (1:1000 in 5% milk in TBS-T). After three washes in 0.1% TBS-T, blot membranes were incubated for 1 h at 23 °C with the appropriate horseradish peroxidase-conjugated anti-rabbit (1:2000 in 5% BSA in 0.1% TBS-T) or anti-mouse (1:1000 in 5% milk in 0.1% TBS-T) secondary antibodies. After three washes in 0.1% TBS-T, the immunocomplexes were visualized by using the enhanced luminol-based chemiluminescent substrate using the Uvitec system (Cleaver Scientific Ltd, UK).

2.7. Preparation of model membranes

The phospholipids DMPC (1,2-dimyristoyl-sn-glycero-3-phosphocholine), d_{54}DMPC (1,2-dimyristoyl-d54-sn-glycero-3-phosphocholine), DOPC (1,2-dioleoyl-sn-glycero-3-phosphocholine 18:1 (Δ9-Cis) PC), sphingomyelin (SM) from egg yolk ≥ 95% purity, Cholesterol (Chol) ≥ 99% purity, Phosphate buffered saline (PBS), and D_2O ≥ 99% purity, were purchased from Sigma Aldrich.

Model membranes were obtained according to the standard thin film deposition protocol [45,46] where the powders of DMPC, d_{54}DMPC, d_{54}DMPC:SM:Chol; 2:1:0.15, and DOPC:SM:Chol; 2:1:0.15, in molar ratio, were weighted separately in glass pear-shaped flasks and dissolved in chloroform. Thin lipid films were deposited on the flasks surface while evaporating the chloroform by the continuous rotation of the flask. Full chloroform evaporation was then achieved under vacuum for 120 mins. Later, the deposited lipid films were put under gentle stream of humidified nitrogen for 60 mins to untangle the multilamellar stacks. The lipid films were then hydrated with the proper buffer required for each technique, and then freezed and thawed for 5 cycles. According to the requirements for each application, some of the prepared model membranes were extruded 51 times through double polycarbonate filters of 80 nm porosity using a manual extruder (LiposoFast, Avestin Inc.) to produce large unilamellar vesicles (LUVs). LUVs were stored above the lipids transition temperature to guarantee the liposomes' stability. According to the requirements of each technique, LUVs were then used as they were, or they were used to deposit supported lipid bilayers (SLBs) as will be described later on.

2.8. Dynamic light scattering (DLS)

The size distribution of the purified EV samples was measured in a quartz cell after being diluted 1:7 in filtered PBS. Measurements were done with a non-commercial DLS system [47] at 90 ° using a Nd:YAG laser source of λ= 532 nm at the temperatures of 25 °C and 37 °C. The measurements have been performed on biological triplicates to ensure reproducibility and were repeated 10 times and analysed by the Non-Negative Least Squares (NNLS) algorithm [48] showing both the intensity and number weighted distributions.

DLS measurements were also executed to assess if the EV interaction with the lipid LUVs affected the LUVs size distribution. Measurements were carried on triplicates and were repeated 10 times, according to the ratio of 5 μL mixed EVs-LUVs sample: 400 μL PBS, filtered. The EVs-LUVs were incubated for 1 h at 45 °C, then measurements were carried at 37 °C and 17 °C, where target LUVs membranes are found, respectively, in the fluid and gel/ordered phase. The 17 °C condition was not intended to reproduce physiological temperature, but was used as a biophysical contrast condition below the DMPC main transition temperature, where the bilayer is more ordered and mechanically rigid. This condition enhances sensitivity to EV-induced perturbations of vesicle hydrodynamic size, lipid-chain packing, and membrane-associated structural changes that may be less apparent in fluid-phase bilayers at 37 °C.

2.9. Nanoparticle Tracking Analysis (NTA)

For measuring the concentrations and size distributions of EVs, a Malvern Panalytical Nanosight NS300 (NanoSight Malvern, Worcestershire, UK) equipped with a scientific complementary metal oxide semiconductor (sCMOS) camera and a blue 488 nm laser was used at 25 °C. A dilution factor of 1:600 was used for all samples and data were read in dynamic mode, acquiring 5 recordings per sample. A camera level of 16 was set for the particle detection, to allow the detection of smaller particles. This configuration allows to clearly show all of the particles in the sample and to have no more than 20% saturated (coloured pixels). Data analysis was performed with Nanosight NS300 NTA software (NanoSight, Malvern, Worcestershire, UK), setting a Particle Detection Threshold of 4 for the tracking analysis of all acquisitions from the three independent experiments, performed on biological triplicates.

2.10. Atomic Force Microscopy (AFM)

For measuring the geometrical diameters and height profiles of the EVs, an MFP-3D Stand Alone AFM (Asylum Research, High Wycombe, UK) was used in the dynamic AC-mode using silicon micro cantilevers (Olympus BL-AC40TS-C2, spring constant k = 0.09 nN/nm). A volume of 30 μl of Poly-L-Ornithine (Sigma-Aldrich, Darmstadt, Germany) was incubated at room temperature for 20 mins on a freshly cleaved mica of 10 mm diameter and 0.15 −0.21 mm thickness (V-1 grade, Nano-Tec). EVs were diluted 1:10 with PBS, and 30 μl of the diluted EVs were incubated for 20 mins on the poly_l_Ornithine treated mica substrate and were then mildly rinsed with 50 μl of PBS. A set of 8 different images with a size of 10x10μm at a lateral resolution of 1024px were recorded on biological triplicates for each type of EVs. A total of 2641 Ctrl and 1869 OligoGM1-EVs were identified in these images. To exclude any outliers or possible aggregates, only the particles with diameters ranging from 30 to 300 nm, with their corresponding heights ranging from 10 to 60 nm were considered for the statistics.

For performing AFM measurements to investigate the interaction of the Ctrl and OligoGM1-EVs with model membranes, a raft model membrane composed of DOPC:SM:Chol; 2:1:0.15 in molar ratio, was used at room temperature. We have previously used this model membrane to study the interaction mode of EVs isolated from mesenchymal cells [14] and EVs isolated from MDA-MB-231 cells. Experiments were repeated 3 times to monitor the preferred interaction route for each type of EVs and their tendency to interact with specific domains of the SLB. A volume of 50 μL of the LUVs raft model membrane with a lipid concentration of 0.25 mg/mL was used for the SLB deposition. After confirming bilayer formation and L_o/L_d phase coexistence by imaging representative pristine areas of the raft SLB, 10 μL of EV suspension (LUVs-EVs number ratio was equivalent to (10^2 : 1)) was deposited onto the SLB. AFM acquisition was started within 5 min after EV addition. A selected post-incubation field (512 ×512 pixel frames) was then imaged

every 10 min to follow the evolution of EV-induced membrane remodelling over time. All AFM data analysis was performed using the free and open-source Gwyddion v2.58 software [49].

2.11. Small and Wide-Angle X-ray Scattering (SAXS and WAXS)

SAXS measurements for the structural analysis of the EV membrane bilayer were measured at the BM26 beamline in the European Synchrotron Research Facility (ESRF) in Grenoble, France. The sample to detector distance was set to 1.4 m, with an X-ray energy of 12KeV, allowing to investigate the scattering-vector range q 0.01–0.6 $Å^{-1}$. A volume of 1.30 µl of each EV sample suspended in PBS were injected into polycarbonate microtube capillaries (ENKI, Italy) and measured at 37 °C. Reference measurements on the empty capillaries and on capillaries filled with PBS buffer have also been performed, to allow for background subtraction. Data were analysed using the SasView-5.0.5 software (https://www.sasview.org) [50], using a multi-shell sphere model with a water core, to describe the bilayer membrane of the EVs as three shells consisting of inner heads, tails, and outer heads layers. Membrane thickness is defined as the sum of the fitted slab thicknesses (inner head + tails + outer head). Fit-derived uncertainties for the individual slab thicknesses were typically ±1 Å. The uncertainty on the total membrane thickness is reported as ±2 Å, based on the fit sensitivity of the derived thickness parameter (i.e., the range over which the total thickness can be varied while maintaining an acceptable fit), and therefore reflects modelling uncertainty.

SAXS and WAXS measurements were also performed for the structural investigation and identification of the form factor of the model membrane liposomes before and after interacting with the EVs. The structural features of the mixed systems and their scattering length density (SLD) profiles could be extracted by modelling the membrane form factor as a series of concentric shells. 2 model membranes were prepared according to the previously explained protocols, the DMPC simple model and the more complex raft model of DMPC:SM:Chol; 2:1:0.15 mol. The LUVs concentration was obtained by considering an area per lipid of 50 Å [2] and a vesicle radius of 60 nm and estimated to be of the order of 10^{14} vesicles/mL for the 20 mg/mL solution. Each 100 µL of the extruded model membrane liposomes (DMPC or Raft models) was incubated separately with a volume of 10 µL of the relevant EVs (Ctrl or OligoGM1-EVs) to a final concentration of 2% in PBS at 37 °C, where the LUVs-EVs number ratio was equivalent to (16 $\times 10^3$: 1).

SAXS data were collected using a Pilatus 1 M detector (DECTRIS, Switzerland, active area: 169 mm × 179 mm) and a Pilatus 300K−W linear detector for WAXS (DECTRIS, Switzerland, active area: 254 mm × 33.5 mm). The samples were injected into polycarbonate capillaries and closed by Teflon caps, then mounted on the sample holder. Temperature was controlled using thermostatic cables connected to the sample holder. Scattering profiles were collected for the empty capillaries and PBS buffer as references, and for the samples, including the model membranes and the mixtures of EVs with the model membranes at 37 °C and 17 °C. These two temperatures were selected to compare the physiologically relevant fluid-phase condition (37 °C) with a lower-temperature, more ordered/rigid membrane state (17 °C), which increases sensitivity to possible EV-induced changes in bilayer form factor and lipid-chain packing. More than 30 measurements for at least 3 batches from each sample (EVs and mixed systems) and references were performed and averaged for providing a good signal-to-noise ratio after comparing the raw scattering curves to each other to ensure there was no trend that may indicate radiation damage to the sample. Data were analysed using the SasView-5.0.5 software.

For SAXS measurements, the scattering profile of the PBS buffer was measured separately and subtracted from the sample's profiles to account for the intensity signal measured from the sample particles alone. The subtraction of the PBS buffer was calculated as a fraction since for each sample's unity of volume, part of it is occupied by the solvent (PBS) and the other part is occupied by the dispersed particles. Thus, the subtraction was carried out as [sample – α*PBS], where α was calculated depending on the concentration of the sample. For WAXS measurements, the scattering from the empty capillaries was subtracted as well to effectively subtract the contribution coming from the molecular structure of the capillary material. The subtraction procedure was carried out as [(sample – α*empty capillary) – β*(PBS -γ*empty capillary)], where α and γ depend on the capillary used, and β depends on the concentration of the sample.

2.12. Small angle neutron scattering (SANS)

The structural alterations occurring in the deuterated d_{54}DMPC LUVs model membrane upon interacting with the EVs were also investigated by SANS. The d_{54}DMPC LUVs were prepared and extruded to a final concentration of 14 mg/mL in PBS prepared in 100% D_2O. The LUVs concentration was obtained by considering an area per lipid of 50 Å [2] and a vesicle radius of 60 nm and estimated to be of the order of 10^{13} vesicles/mL for the 14 mg/mL solution. SANS spectra were first collected from a volume of 600 µL of the bare d_{54}DMPC LUVs in PBS D_2O, then they were mixed with increasing volumes of (10 µL, 20 µL) of the Ctrl and OligoGM1-EVs at 37 °C, equivalent to a LUVs-EVs number ratio of 6 $\times 10^4$: 1, and 3 $\times 10^4$: 1, respectively and left to incubate for 30 min before SANS acquisition. No additional D_2O/H_2O solvent contrasts were collected in this experiment. The 100% D_2O condition was selected to maximize the contrast between the deuterated d_{54}DMPC LUV matrix and the protiated EV-derived components while minimizing incoherent background from H_2O. Accordingly, the SANS-derived SLD changes are interpreted within a single-contrast, comparative framework. All measurements have been performed at a physiological temperature of 37 °C. Multiple measurements were collected from the different samples and, upon checking for reproducibility, have been averaged to get a better signal-to-noise ratio.

Standard quartz microcylindrical Banjo cells with a path length of 2 mm and an average volume of 600 µL were used for the SANS measurements. Data analysis was performed using the SasView-5.0.5 software [50]. The SANS measurements were carried out on the SANS diffractometer "Yellow Submarine" at the Budapest Neutron Centre (BNC) in Budapest, Hungary, over a q-range of 0.005 $Å^{-1}$ - 0.4 $Å^{-1}$. The instrument is equipped with a 64 × 64 pixels (2D) position-sensitive LETI detector filled with BF_3 gas. The instrument control and data acquisition electronics were manufactured by Laboratoire Léon Brillouin, Saclay, France, with in-house data acquisition software [51].

To estimate the relative incorporation of EV-derived material into deuterated LUVs, the fitted scattering length density (SLD) of each bilayer slab j (inner headgroups, hydrophobic tails, outer headgroups) was described using a volume-fraction (ϕ) weighted-sum (mixture) relation:

$$\rho_j^{fit} = \phi_j^{lip}\rho_j^{lip} + \phi_j^{ins}\rho^{ins}\ ,\ \phi_j^{lip} + \phi_j^{ins} = 1 \quad (1)$$

where ρ_j^{lip} is the SLD of the deuterated lipid matrix (bare LUVs), and ρ^{ins} represents the SLD of inserted EV-derived material. This strategy is used for comparative assessment between Ctrl- and OligoGM1-EVs within the adopted contrast assumptions.

2.13. Attenuated total reflection - Fourier transform infrared (ATR-FTIR) Spectroscopy

Molecular profiling of the EVs for estimating their spectroscopic protein/lipid ratio was feasible using the ATR-FTIR technique. ATR-FTIR measurements were acquired on pooled EV material obtained by combining biological triplicates after verifying batch-to-batch reproducibility; repeated acquisitions on the pooled sample yielded reproducible spectra. An approach like that described in the literature [52] was used, where 20 µL of each type of EVs were left for drying on a

multiple-reflection ATR crystal (diamond, 9 reflections). The spectra were measured using a Bruker Vertex 70 FTIR spectrometer at the Chemical and Life Sciences branch of the beamline SISSI (Synchrotron Infrared Source for Spectroscopy and Imaging) [53], at the synchrotron radiation facility Elettra, Trieste, Italy. A Globar was used as the light source, and measurements were performed at room temperature. A series of consecutive spectra were recorded while the sample was left to dry on the crystal. For each spectrum, 256 single spectra recorded at a resolution of 4 cm^{-1} in the range of 5000–530 cm^{-1}, were averaged. The dataset was then pre-processed using the Bruker OPUS 8.5 software package. Spectra were reduced to the range from 4000 cm^{-1} to 530 cm^{-1} while applying an atmospheric compensation to reduce the water vapor and CO_2 contributions.

For the further analysis of the datasets, the Quasar Orange software v.1.10.2 [54] was used. Spectra of the fully dried sample (where spectra do not show major changes) were averaged. Additional post-processing was performed by applying another baseline correction (rubber band, 64 points). As the EV samples were in a PBS buffer solution, the spectra contained spectral features of both the EVs and the PBS. To compensate for that, an attempt was carried out to subtract the spectral contribution of the PBS by measuring the pure PBS buffer solution alone using the identical protocol and subtracting the corresponding spectrum from the EV spectrum. The approach assumed that both solutions contained similar concentrations of EVs and PBS. Moreover, for the final spectra, two flattening procedures (Savitzky-Golay, 2nd degree polynomial with a window size of 19, and a Gaussian smoothing with a standard deviation of 4), as well as a vector normalization were included to make infrared spectral features more readily comparable. Independent from the spectral representation, the analysis of the spectroscopic protein/lipid ratio was carried out using a protocol described by Mihaly et al. [55]. In this case, modification of the spectra was limited, and spectra were used after the buffer subtraction, i.e. without the flattening and vector normalization described beforehand. The area of the Amide I bands ($A_{proteins}$) centred at about 1650 cm^{-1}, and the area (A_{lipids}) of the region from 2700 to 3000 cm^{-1} mostly associated with lipids, were determined through integration. The spectroscopic protein/lipid ratio was then defined as the ratio $A_{proteins}/A_{lipids}$.

Next, to perform the ATR-FTIR measurements for the EV-membrane interaction study, deuterated phospholipid d_{54}DMPC was used as the target model membrane to distinguish the adsorption band of target lipids from that of the eventually inserted lipids from the interacting EVs, with deuterium having a higher mass than hydrogen. A d_{54}DMPC LUVs concentration was obtained by considering an area per lipid of 50 Å [2] and a vesicle radius of 60 nm and estimated to be of the order of 10^{11} vesicles/mL for a 0.1 mg/mL solution. The LUVs-EVs number ratio was equivalent to ($2 \times 10^3 : 1$).

Spectra were measured using the Thermo Nicolet Nexus FTIR instrument at the ISIS Neutron and Muon source, Oxfordshire, UK. The Si ATR crystal was cleaned by sonication for 30 min in 2% (w/v) SDS. It was then rinsed thoroughly with milliQ water and dried under a stream of nitrogen. Then it was UV-Ozone cleaned for 10 min, and washed with milliQ water, and then UV-Ozone cleaned again for 10 min. The crystal was then mounted in a dry flow cell, and the volume was filled with 150 mM NaCl D_2O buffer. A background spectrum was measured for the bare crystal in the buffer, and subtraction spectra were collected for the removal of the water vapor absorbance from the following measurements. Then, for the deposition of the model membrane bilayer, 3 mL of d_{54}DMPC LUVs suspension (0.1 mg/mL) were injected into the measuring cell to deposit a d_{54}DMPC supported lipid bilayers (SLB) on the surface of the Si ATR crystal, at 37 °C. They were let to incubate on the crystal for 20 mins while the IR absorbance spectra were periodically taken through the deposition process until no further spectral changes were observed. The excess unfused liposomes were flushed away using 150 mM NaCl D_2O and the spectrum of the d_{54}DMPC SLB at the Si-buffer interface was recorded, keeping the temperature at 37 °C.

After deposition and characterization of the d_{54}DMPC SLB, a volume of 10 µL of the EVs diluted with 300 µL of PBS D_2O was injected onto the SLB and allowed to interact for 45 mins at 37 °C. The IR absorbance spectra were periodically taken through the interaction process to monitor the interaction and lipid exchange between the EVs and the model membrane. The lipid exchange process between the EVs (Ctrl or OligoGM1) and the d_{54}DMPC model membrane was measured as the H/D exchange monitored by performing integrations of the Aliphatic C-Dx peaks (C-D_3 and the symmetric/ asymmetric C-D_2 bands) of the d_{54}DMPC model membrane tails region at 2300–2000 cm^{-1} which were decreasing with time, relative to the Aliphatic C-Hx peaks of the EVs at 3100–2800 cm^{-1} (C-H_3 and the symmetric/ asymmetric C-H_2 bands). Data analysis was performed using the OMNIC 9.2.86 instrument software and OriginPro 2023b. Experiments have been repeated and results have found to be reproducible.

2.14. Neutron reflectometry (NR)

NR provides laterally averaged isotopic composition of planar samples along their plane-perpendicular direction with nanometer resolution. Hence, NR spectra were collected to reveal the transverse structure of the SLB models upon their interaction with both types of EVs and to investigate the possible protein intercalation from the Ctrl and OligoGM1-EVs into these model membranes. For these experiments, two model membranes were examined: the simple membrane model made of DMPC, and a deuterated raft (dRaft) model made of the ternary mixture of d_{54}DMPC:SM:Chol; 2:1:0.15 in molar [45]. The NR silicon substrate was first thoroughly cleaned using SDS, acetone, chloroform, ethanol, and then finally it was UV-ozoned for 30 mins. LUVs of the two model membranes were diluted to a final concentration of 0.5 mg/mL just before incubation in the NR measurement cells for the supported lipid bilayer (SLB) deposition process. NR spectra were all collected at 37 °C. For the DMPC model membrane, measurements have been performed in 2 water mixtures with different scattering length densities (SLDs): H_2O PBS and D_2O PBS. While for the dRaft model membrane, NR spectra were collected in 3 solvent mixtures with different SLDs, in H_2O PBS, in SiMW (Silicon Matched Water) PBS (i.e., a mixture of H_2O:D_2O; 62%:38% where the SLD is equal to that of Silicon), and in D_2O PBS.

For both types of model membranes, the interaction of both types of EVs was examined by injecting a volume of 20 µL of EVs (Ctrl-EVs or OligoGM1-EVs) onto each cell where the SLB model was previously characterized by NR, with a LUVs-EVs number ratio equivalent to ($6 \times 10^3 : 1$). EVs were incubated for 1 hr with the target model membranes; then the cells were carefully washed with the relevant buffer to remove any unfused EVs, and the NR spectra in the previously mentioned different solvent mixtures were collected again. The NR measurements were performed at the Offspec vertical reflectometer at the ISIS Neutron and Muon Source, Oxfordshire, UK, in the time-of-flight (TOF) mode at 37 °C. Reflectivity data were collected using a wavelength band from 1.5 to 14 Å at two incident angles of 0.6 ° and 2.3 ° covering a q_z range of 0.009–0.33 $Å^{-1}$ at a constant dq_z/q_z resolution of 4%. Collected spectra were normalised by the spectrum for the incident beam collected in transmission through the Si substrate. The NR data analysis was carried out using the open-source Python script (anaklasis) [56] according to the protocol described in [45]. Briefly, it enables the calculation of the parameters characterizing the different layers constituting the model membrane, such as the thickness, SLD, roughness, and solvent penetration.

The NR spectra were modelled as successive layers of silicon bulk, silicon oxide (SiO_2), water layer, and the SLB model ordered as inner heads, inner tails, outer tails, outer heads, and finally the outer bulk water. Spectra obtained in the different solvents having different SLDs, were contemporarily fitted. For the estimation of confidence intervals of the fitted model parameters and for identifying any potential correlations between free parameters, we performed a Bayesian MCMC sampling of the system as implemented in the Anaklasis package. The SLD of the DMPC head group is $1.87 \times 10^{-6} Å^{-2}$, and that of the DMPC tails

-0.39×10^{-6}Å^{-2}, while the H-bringing EVs have average SLD values of their protein components and lipids equal to Å^{-2} and -0.4×10^{-6} Å^{-2}. Therefore, benefitting from the contrast difference between the SLD of the hydrophobic tails of the DMPC SLB model and the proteins coming from the EVs, an estimation of the proteins insertion from EVs into the SLB could be done, while lipid insertion from the EVs or exchange between the mixed systems couldn't be monitored. On the other hand, the dRaft SLB composed of the ternary mixture of d_{54}DMPC/SM/Chol, has an average SLD value of the polar heads and tails layers equal to 1.7×10^{-6} Å^{-2} and 4.25×10^{-6} Å^{-2}, and thus an alteration of that regions SLD values can indicate both lipid and protein insertions from the EVs: upon interaction they will cause an increase in the SLD of the SLB hydrophilic heads layer and a decrease of the SLD of its hydrophobic tails.

2.15. Differential scanning calorimetry (DSC)

DSC measurements were applied to study the changes in the thermotropic behaviour of model membranes in the form of LUVs upon their interaction with the EVs. For these experiments, two model membranes were tested, a simple 1-component model made of DMPC alone, and a raft model made of a mixture of DMPC:SM:Chol; 2:1:0.15 in molar ratio. We have previously also used this model membrane to study the interaction mode of EVs isolated from mesenchymal cells [16,17]. The DMPC LUVs concentration was obtained by considering an area per lipid of 50 Å [2] and a vesicle radius of 60 nm and estimated to be of the order of 10^{14} vesicles/mL for the 20 mg/mL solution in PBS buffer. 200 μL of LUVs were mixed with increasing volumes of each type of EVs (5 μL, 10 μL, and 20 μL) where the LUVs-EVs number ratio was equivalent to (6×10^4 : 1, 3×10^4 : 1, 1.5×10^4 : 1). Glass capillaries were weighted before and after being filled with the samples and securely sealed with a blowtorch. Measurements were carried out using a MASC calorimeter [57]. Samples underwent temperature cycles ranging from 15 to 50 °C at a scan rate of 1 °C / 3 mins, in both cooling and heating modes, with an initial 1 h isotherm at 50 °C. Afterwards, intermediate isotherms of 1 h were set before each cooling and heating cycle. Repeated measurements yielded consistent results.

2.16. Statistical analysis

The physicochemical characterization of extracellular vesicles (EVs) was performed using biological triplicates, with each experiment conducted at least three times to ensure robust reproducibility. For the membrane interaction assays, pooled EV material was employed once the physicochemical properties were confirmed to be consistently reproducible. These interactions were occasionally repeated multiple times, depending on the specific technique used, and the data derived from these experiments are presented as spatial averages.

For DLS, the primary hydrodynamic diameter (Z-average) and polydispersity index (PDI) were calculated from the cumulant fit of the intensity autocorrelation function. The standard measurement error is expressed as the standard deviation (SD) across the triplicate means. Furthermore, to characterize the presence of multiple size populations, the Non-Negative Least Squares (NNLS) algorithm [48] was applied to the correlation data to extract both intensity- and number-weighted size distributions. For the NTA, data were expressed as means ± SEMs and were analysed for significance by the unpaired T-test. The analysis was performed with Prism software 10.3.0 (GraphPad Software, Inc., La Jolla, CA, USA; https://www.graphpad.com/). A p value < 0.05 was considered significant. For AFM, the final geometrical diameters and heights for each EVs type were calculated from the refined datasets described previously, with the measurement error expressed as the standard deviation (SD) across the biological triplicates. Moreover, due to the nanoscale size of the EVs-induced protrusions observed in AFM images, a conventional statistical analysis of their height distribution was not feasible. Specifically, these features are laterally confined to only a few pixels, making height determination highly sensitive to pixel resolution and tip convolution effects. In addition, the protrusions were found to be mechanically unstable under scanning conditions, frequently undergoing rearrangement or deformation upon interaction with the AFM tip. This prevents reproducible measurement of individual features and introduces significant uncertainty in height extraction. For these reasons, quantitative analysis based on mean values and standard deviations would not be statistically robust. Instead, the reported height represents a representative estimate derived from multiple independent observations across different regions and samples. The apparent association of EV docking sites with L_o, L_d, or L_o/L_d boundary regions was assessed qualitatively from AFM topography. A statistically robust phase-partitioning analysis was not possible because L_o and L_d regions are identified from their relative height, while EV docking and the associated local membrane remodelling alter or obscure this height contrast at the interaction site. In addition, pristine SLB images used to verify L_o/L_d phase coexistence were acquired from different membrane areas than the post-EV interaction images and therefore could not be registered to reconstruct the underlying phase before docking. Consequently, the AFM data are used only to identify reproducible qualitative patterns of domain association, and no quantitative L_o/L_d partition coefficient or statistically established domain preference is reported.

For SAXS, data were analysed using the SasView-5.0.5 software [50]. As the scattering curves were averaged across multiple measurements to optimize the signal-to-noise ratio prior to modelling, the errors for the extracted structural parameters (thicknesses and SLDs) represent fit-derived uncertainties. These values reflect the sensitivity of the fitting algorithm, defining the strict range over which a parameter can be varied while still maintaining the best mathematically acceptable fit. Consistent with the SAXS analysis, SasView-5.0.5 software was again used for fitting the SANS data. Here, the relative incorporation of two increasing volumes of Ctrl- and OligoGM1-EVs into the deuterated DMPC model membrane was quantified. The uncertainties reported for these fitted SLDs and resulting volume fractions correspond strictly to the fit-derived errors, reflecting the sensitivity limits of the mathematical model applied to the averaged scattering data.

For the protein/lipid ratio calculated by FTIR, the error was estimated based on the standard deviation (SD) of the integrated curve of the dried sample for the protein and lipid bands for 10 (Ctrl-EVs) and 14 (OligoGM1-EVs) spectra recorded after drying, respectively. The error of the ratio was determined according to standard error propagation.

For interpreting the kinetics of EVs interaction with the deuterated model membrane by ATR-FTIR, data analysis was performed using OMNIC 9.2.86 and OriginPro 2023b software. Experiments were repeated to verify reproducibility. For quantitative assessment of the lipid exchange kinetics, the relative integrated peak areas (C-Hx / C-Dx) at each time point were averaged across the replicates, with the measurement error expressed as the standard deviation (SD).

For NR, spectra obtained in the different solvents having different SLDs were contemporarily fitted. To estimate the confidence intervals of the fitted model parameters and identify any potential correlations, Bayesian Markov Chain Monte Carlo (MCMC) sampling was performed as implemented in the Anaklasis package. Consequently, the final reported errors for all structural parameters (thickness, SLD, roughness, and solvent penetration) do not represent experimental standard deviation, but rather the fit-derived uncertainties, defined by the confidence intervals of the posterior distributions from this Bayesian sampling.

Finally, for DSC, the reported phase transition temperatures (T_m) and their corresponding shifts (ΔT_m) for both inner and outer leaflet-associated peaks are presented as the mean ± standard deviation (SD). This uncertainty was estimated from repeated, successive thermal scans of the same sample under identical conditions, thereby encompassing both instrumental run-to-run variability and the algorithmic uncertainty inherent to the peak-fitting and peak-picking procedures.

3. Results

To investigate whether OligoGM1 treatment of N2a-derived cells alters the properties of the secreted extracellular vesicles (EVs) and their coupling to lipid membranes, we adopted a two-step experimental design (Fig. 2). First, we characterized Ctrl- and OligoGM1-derived EVs populations using complementary methods to quantify size/distribution and to probe molecular composition and membrane bilayer structural parameters. Second, we evaluated their interactions with biomimetic membranes (supported lipid bilayers and LUVs) using orthogonal surface- and depth-sensitive readouts of docking, remodelling and material exchange.

3.1. Physico-chemical properties of EVs

3.1.1. EVs concentration and size distribution

EVs purity was validated by enrichment of ALIX, TSG101, and CD9 and absence of calnexin [1,2] (Fig. S1). Further characterization was performed using a multi-technique approach combining NTA, DLS, and AFM [13,58] for size distribution, ATR-FTIR [52,55] for compositional description and SAXS for structural investigation [14,59–61].

EVs preparations are intrinsically polydispersed and their size is therefore better described through distribution metrics rather than a single mean diameter. Accordingly, we report size and heterogeneity using complementary descriptors from orthogonal techniques. NTA provides the full particle-size distribution (i.e. EVs diameter) and its characteristic values, whereas DLS yields an intensity-weighted hydrodynamic diameter together with the polydispersity index (PDI) as a standard measure of distribution breadth.

NTA (Fig. 3**a**) and DLS (Fig. 3**b**) measurements revealed comparable hydrodynamic diameter distributions for Ctrl- and OligoGM1-EVs (~130–140 nm) with narrow distributions as evidenced by the DLS PDI values (0.18 ± 0.06 and 0.18 ± 0.04 for the Ctrl- and OligoGM1-EVs, respectively), OligoGM1-EVs having size distribution centred around slightly lower values.

The Ctrl-EVs mean diameter determined by NTA at 25 °C was equal to 140 ± 15 nm at the mode of 109 ± 10 nm and a width of distribution SD= 58 ± 10 nm. While after treating the N2a cells with OligoGM1, the resultant OligoGM1-EVs were found to have a slightly smaller hydrodynamic diameter of 134 ± 13 nm at the mode of 106 ± 9 nm with SD= 51 ± 8 nm. The intensity-based DLS analysis of the 2 types of EVs, showed similar hydrodynamic diameter distributions at 25 °C of 138 ± 24 nm and 131 ± 23 nm for the Ctrl- and OligoGM1-EVs, respectively. A more detailed analysis of the differences between the DLS intensity-based and number-based size distribution measurements at 25 °C and 37 °C is shown in the SI (SI Figs. S2, S3 and Table S2**).** The comparable EVs' size distribution was further confirmed by AFM showing geometric diameters of (~65–70 nm ± 39 nm), consistent with the reduced footprint of EVs on solid supports (SI Figs. S4, S5 and Table S3) [14,15,58,62]. AFM confirmed also that among the two vesicles populations, OligoGM1-EVs are the ones centred around slightly lower values. Noteworthy, DLS yields a narrower size distribution (i.e. lower PDI) due to its intensity-weighted bias toward larger, fully hydrated vesicles, whereas AFM captures the true sample polydispersity and broader variance caused by the physical flattening of soft vesicles onto a rigid substrate.

While Ctrl- and OligoGM1-EVs display comparable overall diameter distributions, OligoGM1-EVs exhibit a modest yet reproducible size reduction of approximately 5% (Table S3). Orthogonal size characterization via DLS, NTA, and AFM yielded expected technique-dependent variations in absolute values. Specifically, solution-state hydrodynamic diameters were systematically larger in DLS than NTA due to the inherent bias of intensity-weighted ensemble averaging ($I \alpha r^6$) compared to number-weighted particle tracking, though both fluid-phase methods confirmed population homogeneity. In contrast, solid-state AFM topography yielded significantly smaller geometric diameters and broader variances, reflecting the physical deformation and flattening of the soft EV bilayers onto the rigid substrate. Importantly, despite these fundamentally distinct physical principles and measurement environments, the relative 5% size reduction of OligoGM1-EVs was consistently preserved across all platforms. This robust cross-platform agreement firmly supports the conclusion that the two EV populations are not identical at the population level. Though modest, this rigorously validated dimensional shift motivated the subsequent deeper structural assessment.

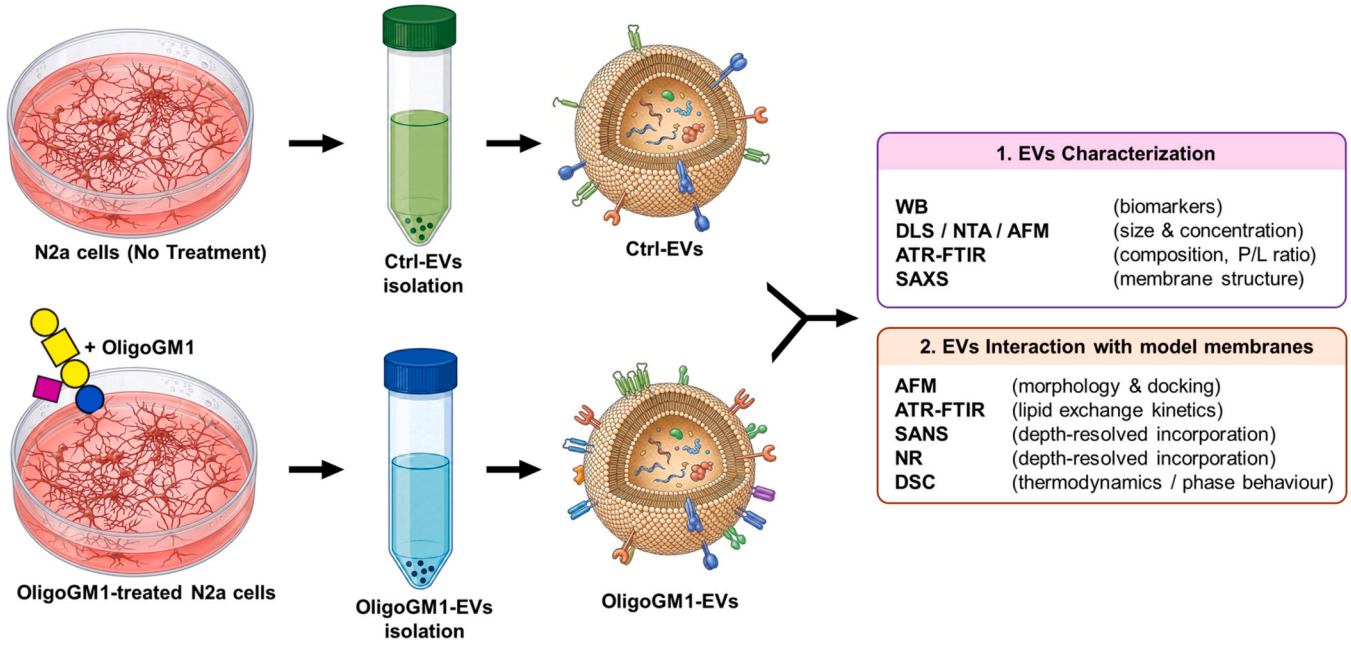


Fig. 2. Schematic workflow of the work: N2a cells treatment with OligoGM1, subsequent EV secretion, EV isolation, and the downstream characterization/interaction assays comparing to EVs secreted from untreated N2a cells.

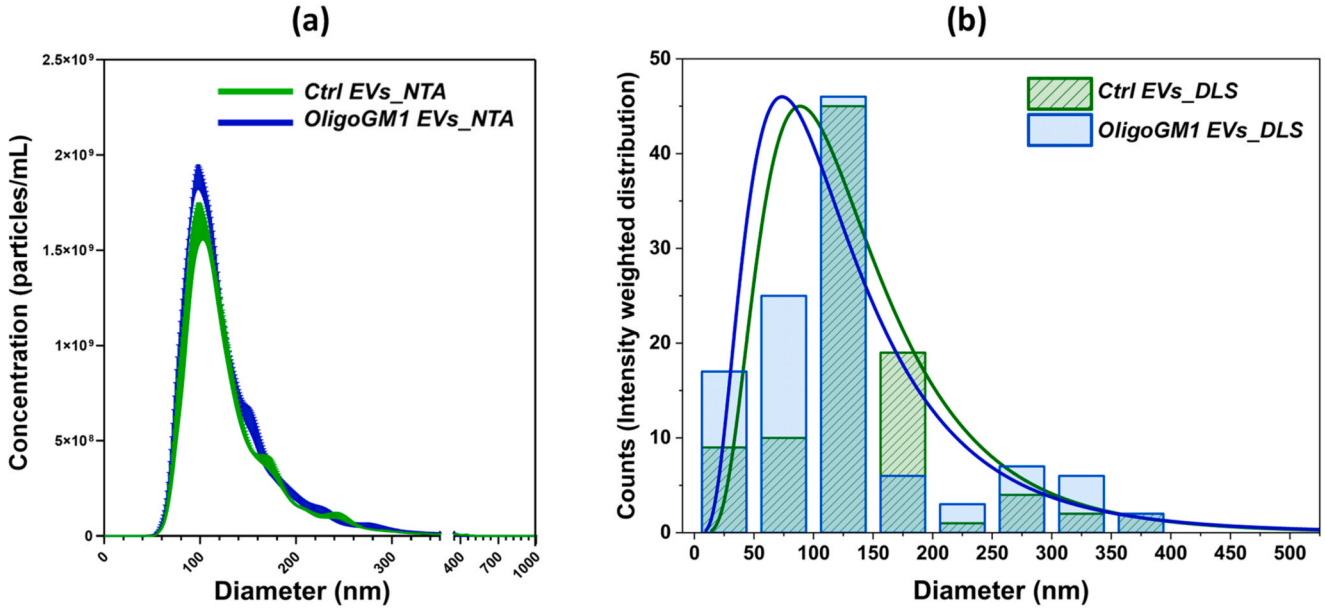


Fig. 3. Comparison of size distribution (i.e. EVs diameter) and concentration of Ctrl-EVs and OligoGM1-EVs by NTA in (a) and DLS in (b), for measurements at 25 °C. (a) the NTA measurements are representative of at least three independent experiments (n = 3) on biological triplicates. A two-tailed analysis indicated statistical significance ($p < 0.0001$). (b) the DLS images are representative of at least three independent experiments (n = 3) on biological triplicates, showing the Log-normal intensity-weighted size distribution comparison between Ctrl-EVs and OligoGM1-EVs.

3.1.2. Compositional and structural differences revealed by ATR-FTIR and SAXS

To evaluate potential treatment-induced alterations in the biochemical composition of the EVs, ATR-FTIR spectroscopy was performed. Data show that OligoGM1-EVs possess a lower spectroscopic protein-to-lipid ratio (0.438 ± 0.005 vs. 0.482 ± 0.003 for the Ctrl-EVs, obtained from the integrated Amide I band region at ≈1657 cm^{-1} vs. the lipid contributions at ≈2700–3000 cm^{-1}) (SI, Fig. S6). The lower protein-to-lipid spectroscopic ratio observed by ATR-FTIR, indicating a shift in the global protein/lipid balance of OligoGM1-EVs, is consistent with relative lipid enrichment and/or a reduced contribution from luminal/soluble proteins; however, ATR-FTIR alone cannot uniquely discriminate between these two contributions. In addition, differences in CH_2 stretching modes (2923 and 2852 cm^{-1}) suggested altered acyl chain order and packing.

SAXS analysis (Fig. 4**a**) was therefore carried out to unveil the nanoscale structure of the two EVs populations. The SAXS profiles show the typical bilayer form factor, with a curvature at scattering vector

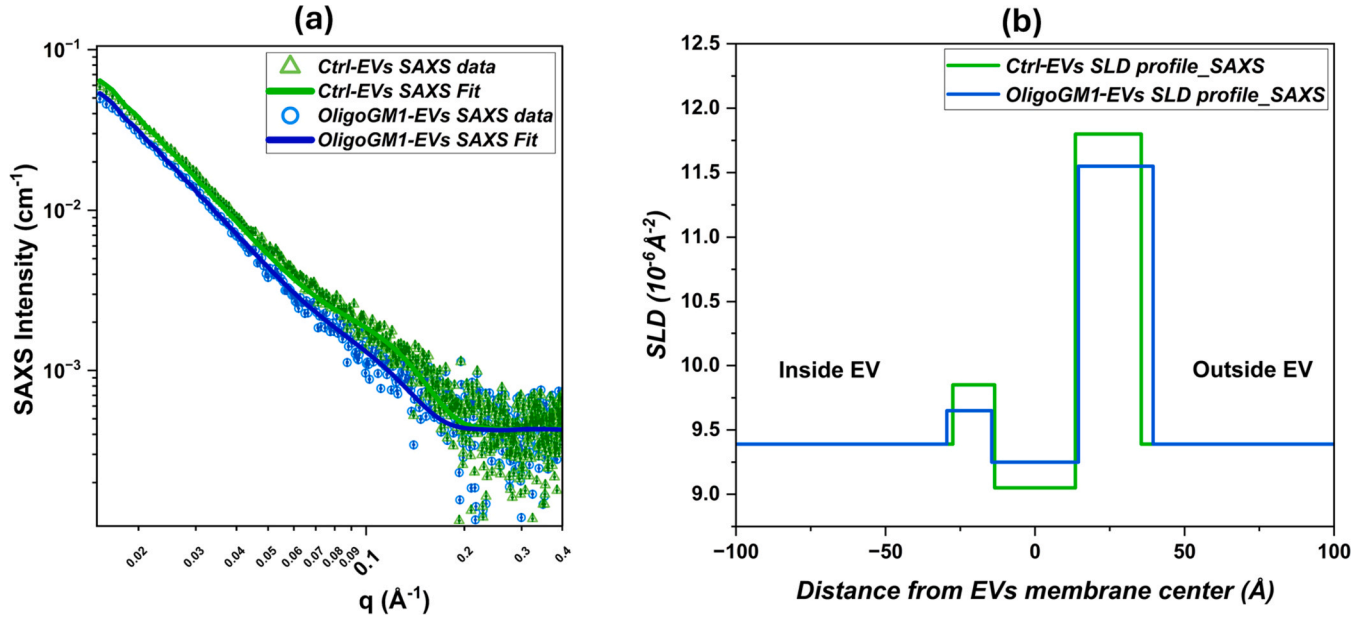


Fig. 4. (a) SAXS profiles and corresponding best fits for Ctrl-EVs and OligoGM1-EVs measured at 37 °C. Error bars represent the uncertainty from SAXS data reduction (counting statistics and background subtraction). Solid lines are best-fit curves from the three-shell bilayer model; green denotes Ctrl-EVs and blue denotes OligoGM1-EVs. Fitted parameters and fit-derived uncertainties are reported in SI Table S4. (b) Scattering length density (SLD) profiles of the EVs obtained from a three-shell membrane model; green denotes Ctrl-EVs and blue denotes OligoGM1-EVs.

$q \approx 0.1$ Å^{-1} indicative of membranes with a thickness of about 6 nm. Modelling the data using a three-shell bilayer (Fig. 4**b**) is consistent with the presence of dispersed vesicular structures possessing a membrane thickness of 63 ± 2 Å for Ctrl-EVs and of 69 ± 2 Å for OligoGM1-EVs (Table S4). We note that repeated SAXS acquisitions yield superimposable scattering profiles, whereas the reported uncertainties on structural parameters reflect fit-derived modelling uncertainties rather than run-to-run variability. Based on SLD values available in the literature for proteins (11.8×10^{-6}Å^{-2}), phospholipids (14.5×10^{-6}Å^{-2}) and cholesterol (8.2×10^{-6}Å^{-2}) [63], we estimated a higher fraction of membrane-embedded proteins in OligoGM1-EVs (~5% relative increase). Both EVs types also exhibited leaflet asymmetry, typical of endosome-derived vesicles [14].

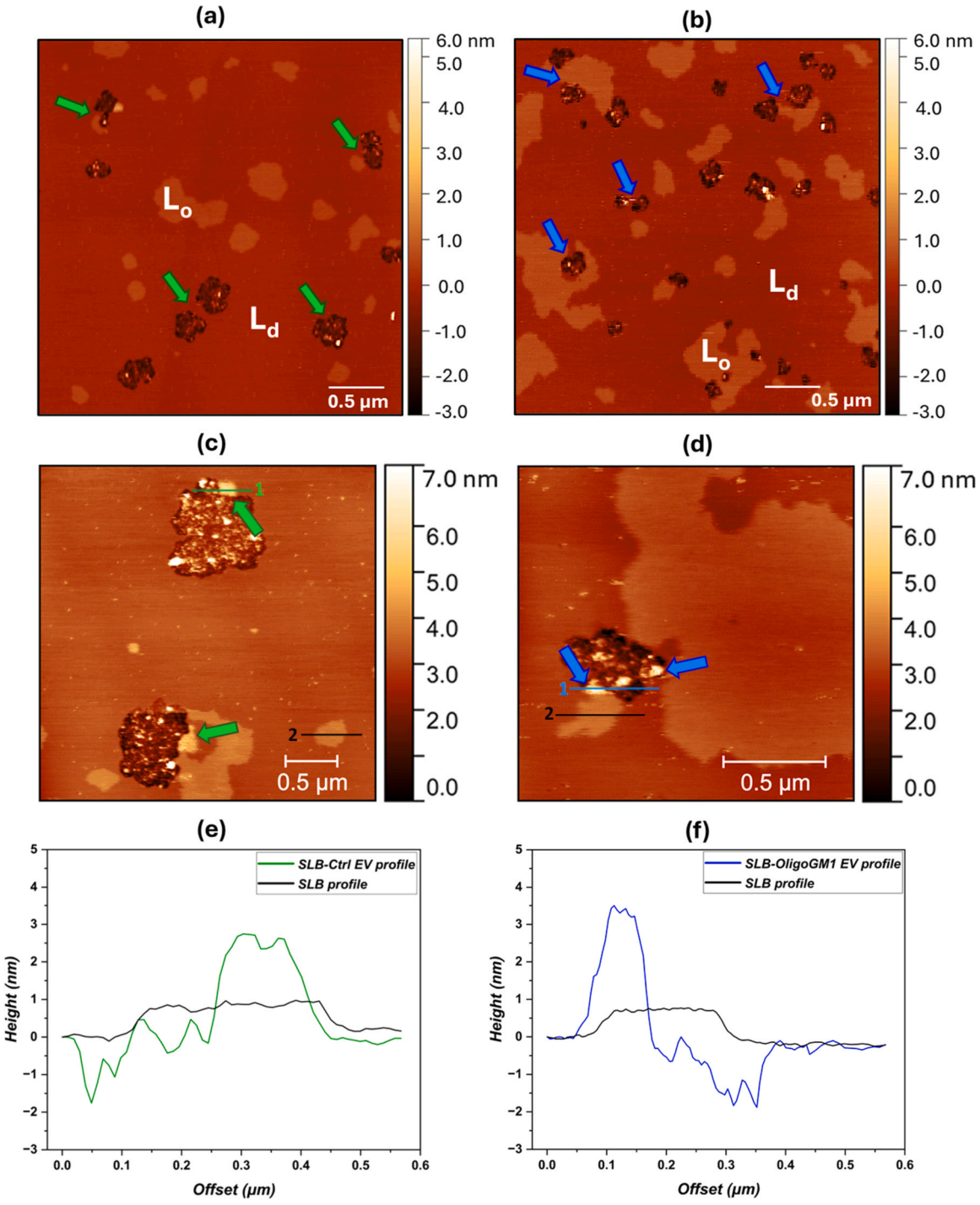


Fig. 5. AFM topographic images of the EVs interacting with the raft model of DOPC:SM:Chol, 2:1:0.15 mol, SLB deposited in 100 mM NaCl buffer at room temperature. (a) Interaction of the Ctrl-EVs with the SLB, green arrows indicate representative Ctrl-EVs interaction sites observed in both L_o- and L_d-associated regions (b) Interaction of the OligoGM1-EVs with the SLB, blue arrows are pointing at their preferential docking sites mainly at the L_o/L_d boundaries. (c) Initial docking sites of the Ctrl-EVs with the SLB. (d) Initial docking sites of the OligoGM1-EVs with the SLB. (e) and (f) Corresponding line profiles for the SLB with the Ctrl and Oligo-GM1 EVs, respectively, showing protrusions at the EVs' docking sites up to 2.7 ± 0.2 nm for Ctrl-EVs and 3.2 ± 0.2 nm for OligoGM1-EVs.

3.2. Nanoscale interaction of EVs with raft-like bilayers

DMPC was used as the reference phosphatidylcholine matrix, enabling component-resolved measurements across multiple techniques. Although DMPC is not the most compositionally representative PC in mammalian plasma membranes, it provides (i) an accessible main transition temperature for controlled thermotropic probing and DSC analyses, (ii) fluid-phase bilayers at 37 ° C, and (iii) crucially, ready availability of matched protiated and deuterated forms, which is essential for isotopic-contrast approaches (ATR-FTIR on deuterated SLBs and neutron scattering/reflectometry) that discriminate target-membrane lipids from EV-derived components. To complement this platform system with a more biomimetic context, we also employed raft-like/phase-separating membrane compositions (e.g., DOPC:SM:Chol and deuterated raft SLBs) to assess domain-selective interactions by complementary techniques.

3.2.1. AFM analysis of EVs and Supported Lipid Bilayer (SLB) interaction

To visualize early EV–membrane engagement, we performed AFM imaging on SLBs containing coexisting liquid-ordered (L_o) and liquid-disordered (L_d) domains (DOPC:SM:Chol, 2:1:0.15 molar ratio) at room temperature. This system emulates key features of neuronal membranes, as the presence of lower fluidity, raft-like domains [64–68]. Boundaries between L_o and L_d domains (i.e. L_o/L_d boundaries), form a line of thickness mismatch, a free energy minimum which constitutes an energetically favourable interaction site for macromolecules/nanovesicles, even in the absence of large curvature deformations [14,69]. This membrane model has been extensively validated in previous studies for probing EV–membrane interactions [14,15].

AFM images acquired within 5 min after EV incubation on the SLBs (Fig. 5 and Figs S7,S8) showed that both EV populations rapidly interacted with the heterogeneous membrane surface. Across repeated experiments, OligoGM1-EV interaction sites were frequently observed in close association with L_o/L_d boundaries, whereas Ctrl-EV interaction sites appeared more broadnt rather than as a quantitatively established domain ly distributed over the heterogeneous bilayer. Because L_o and L_d phases are distinguished by their relative topographic height, local EV docking and membrane remodelling obscure the height contrast required for an unambiguous assignment of the underlying phase.

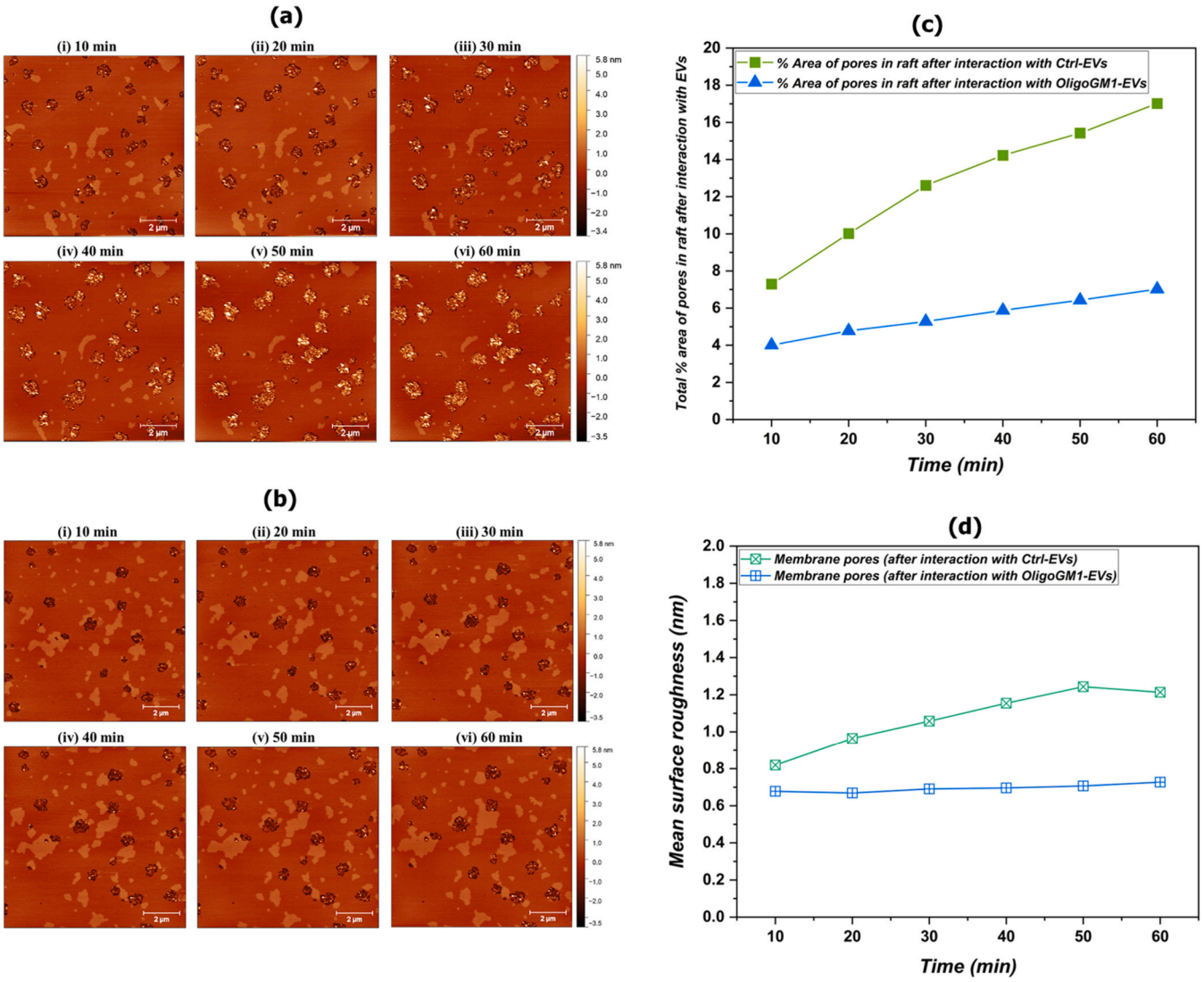


Fig. 6. AFM topographic images following the interaction process of the Ctrl-EVs (panel a) and OligoGM1-EVs (panel b) with a DOPC:SM:Chol; 2:1:0.15 raft SLB in 100 mM NaCl, upon time, at room temperature. Images a(i-vi) show the same field size with a timelapse of 10 mins for the Ctrl-EVs interaction sites. Images b(i-vi) show the same field size with a timelapse of 10 mins for the OligoGM1-EVs interaction sites. Field size = 10 × 10μm, Resolution= 512 × 512 pixels. (c) Percentage of the area covered by pores observed in (a) and (b) induced by the interaction of Ctrl and OligoGM1-EVs with the raft SLB; (d) Evolution of the mean surface roughness observed in (a) and (b) of the Ctrl and OligoGM1-EVs interaction sites with the raft SLB model, upon time.

Moreover, pristine and post-interaction images were acquired from different membrane areas. Therefore, this observation is interpreted as a qualitative difference in the spatial pattern of membrane engagement rather than as a quantitatively established domain preference. Upon docking, EVs induced nanoscale protrusions and shallow depressions, likely corresponding to component exchange or lipid withdrawal (Fig. 5**c,d**). The depth of the pores (~3 nm, Fig. 5**e,f**) is consistent with membrane fluidization and lipid extraction from the outer leaflet of the SLBs [14,15]. Since the observed protrusions are laterally very small, spanning only a few pixels in the AFM images, and are not mechanically stable under scanning conditions, more accurate statistical analysis could have not been performed.

Time-lapse images (Fig. 6) were also analysed using an image masking protocol generated in Gwyddion (Fig. 6, and Figs S9-S12) [14, 15]. They showed different behaviour of the two EVs populations: rapid pore expansion, coalescence of disrupted regions, and steadily increasing surface roughness (Fig. 6**c, d**) in the case of Ctrl-EVs, consistent with extensive deposition and membrane remodelling; while there was slow and spatially confined pore formation with minimal roughness evolution for OligoGM1-EVs (Fig. 6c,**d**).

3.2.2. *Model membrane remodelling in solution (DLS, SAXS, WAXS)*

Complementary biophysical techniques as DLS, SAXS and WAXS were applied to further examine the molecular mechanisms underlying membrane remodelling upon EV exposure, in the absence of a support. LUVs, using DMPC alone or DMPC:SM:Chol; 2:1:0.15 (i.e. raft-LUVs), were employed.

To compare EV–LUV interactions under different membrane-ordering regimes, mixed systems were analysed at 17 °C and 37 °C. The 17 °C condition was used as a low-temperature, gel/ordered-phase contrast condition for DMPC-containing LUVs, whereas 37 °C represents the physiologically relevant fluid-phase condition. DLS measurements for the mixed systems of the EVs with the DMPC and raft LUVs at 17 °C and 37 °C are shown in the SI**,** Fig. S13 and Table S5**.** When incubated with DMPC or raft-LUVs, both EV types increased the LUV hydrodynamic diameter at 17 °C. OligoGM1-EVs produced a more pronounced effect in raft-LUVs, consistent with the qualitatively different spatial interaction pattern observed by AFM on phase-separated SLBs. We recall that DLS reports an effective hydrodynamic size distribution of the dominant scattering objects in solution and does not, by itself, resolve a unique molecular mechanism. Accordingly, the modest diameter increase observed at 17 °C is consistent with EV–LUV association/adhesion and/or limited transfer of EV-derived components to the LUV membrane, which can modify vesicle surface composition and apparent curvature/roughness and thus increase the measured hydrodynamic diameter. At physiological temperature (37 °C), the LUV hydrodynamic diameter did not change significantly within the sensitivity of DLS. Since DLS reports an effective, diffusion-derived mean size, subtle interfacial remodelling in fluid-phase bilayers may occur without producing a measurable shift in the intensity-weighted diameter.

SAXS and WAXS measurements at the same two temperatures were used to assess whether these DLS-detected changes were accompanied by larger-scale modifications of bilayer form factor or acyl-chain packing.

SAXS on mixed LUVs-EVs systems revealed minimal changes of the LUVs bilayer form factor upon interaction (Fig. S14), both in the case of DMPC-LUVs and raft-LUVs, indicating that neither Ctrl- nor OligoGM1-EVs dramatically disrupt bilayer thickness or overall lamellar organization. This is consistent with the partial components mixing inferred from AFM.

Moreover, WAXS measurements showed that chain packing within the LUVs hydrophobic core (Fig. S15) remained unchanged upon EVs exposure, indicating no large-scale disruption. These findings align with SAXS results and suggest that EV-induced remodelling primarily affects outer leaflet composition and lateral organization rather than global bilayer packing.

Overall, the comparison between 17 °C and 37 °C indicates that EV-induced changes are more readily detected in ordered/rigid DMPC-containing bilayers, whereas in fluid-phase membranes at physiological temperature the interaction may proceed through subtler interfacial rearrangements or component exchange without producing large-scale changes in vesicle size, bilayer form factor, or acyl-chain packing.

3.2.3. *Quantitative depth profiling of EV insertion (SANS)*

To resolve how deeply EV components penetrate target membranes, we performed SANS on deuterated d_{54}DMPC LUVs. Deuteration strengthen the contrast between the LUV matrix and the protiated components delivered by EVs, enabling sensitive detection of protein and lipid insertions within the bilayer.

SANS spectra of bare d_{54}DMPC LUVs displayed the expected form factor characteristic of fluid-phase phosphatidylcholine bilayers. Upon incubation with increasing volumes of either Ctrl- or OligoGM1-EVs (10 and 20 μL), systematic changes in the scattering profiles were observed (Fig. 7**a,b**). Fitting the data using a multilayer spherical-shell model allowed to infer the scattering length density (SLD) profiles for the inner headgroups, hydrophobic tails, and outer headgroups (Fig. 7**c,d**; SI Fig. S16 and Tables S6,7). Given the ensemble-averaged nature of SANS, alternative microscopic scenarios (e.g., surface-associated deposits versus bilayer incorporation) cannot always be uniquely discriminated unless they produce a sufficiently uniform contrast signature; we therefore interpret the fitted SLD changes as consistent with relative EV-derived material incorporation within the sensitivity of the method.

A progressive thickening of the hydrophobic core—from 26 ± 1 Å in bare LUVs to 29 ± 1 Å at the highest EV dose—was observed for both EV populations. Alongside, the SLD of the hydrophobic tails decreased from $6.80 \pm 0.05 \times 10^{-6}$ Å^{-2} to $6.66 \pm 0.05 \times 10^{-6}$ Å^{-2} (for Ctrl-EVs) and to $6.73 \pm 0.05 \times 10^{-6}$ Å^{-2} (for OligoGM1-EVs). Within the contrast and resolution of SANS, the fitted SLD changes are consistent with an ensemble-average incorporation of EV-derived (protiated) material into the LUV bilayer, enabling a relative comparison of the extent of bilayer incorporation between Ctrl- and OligoGM1-EVs.

Both the inner and outer headgroup layers showed increased SLD following EV exposure, indicating that EV components penetrated both leaflets of the LUV bilayer. Notably, the magnitude of these changes differed between the two EV types. Ctrl-EVs induced a stronger increase in headgroup SLD and a more pronounced decrease in tail SLD, reflecting greater incorporation of protiated material. Quantitatively, knowing that the average SLD of a protein in D_2O is equal to 2.5×10^{-6} Å^{-2} [63], protein insertion volumes were estimated at ~8% and ~15% for Ctrl-EVs compared to ~3% and ~8% for OligoGM1-EVs for the 2 increasing EV doses. These values represent relative differences between EV populations rather than absolute insertion efficiencies.

3.2.4. *Lipid Exchange dynamics quantified by ATR-FTIR*

Lipid exchange dynamics were monitored by means of ATR-FTIR spectroscopy on supported d_{54}DMPC bilayers at 37 °C, where d_{54}DMPC is in its fluid phase. As before, deuterated lipids were used to enable a clear spectral discrimination between SLB-derived signals (C–D stretching region ≈ 2275–2025 cm^{-1}) and protiated lipids delivered by EVs (C–H stretching region ≈ 3075–2750 cm^{-1}). ATR-FTIR probes the near-surface interfacial region within the evanescent-field sampling depth and does not provide leaflet-specific information. Therefore, changes in the C–D and C–H bands will be interpreted as net depletion/displacement of deuterated SLB lipids and net accumulation of protiated EV-derived lipids within the probed interfacial region, without uniquely assigning the signal to the SLB outer leaflet versus EV-derived bilayer material bound at the surface.

Upon interaction of both types of EVs with the SLB, the intensity of the C–D stretching bands decreased progressively (Fig. 8**a,b**), indicating removal or displacement of d_{54}DMPC lipids from the SLB. Real-time measurements revealed that Ctrl-EVs rapidly extracted ~20 ± 1% of SLB lipids within 15 min while partially compensating for this loss by

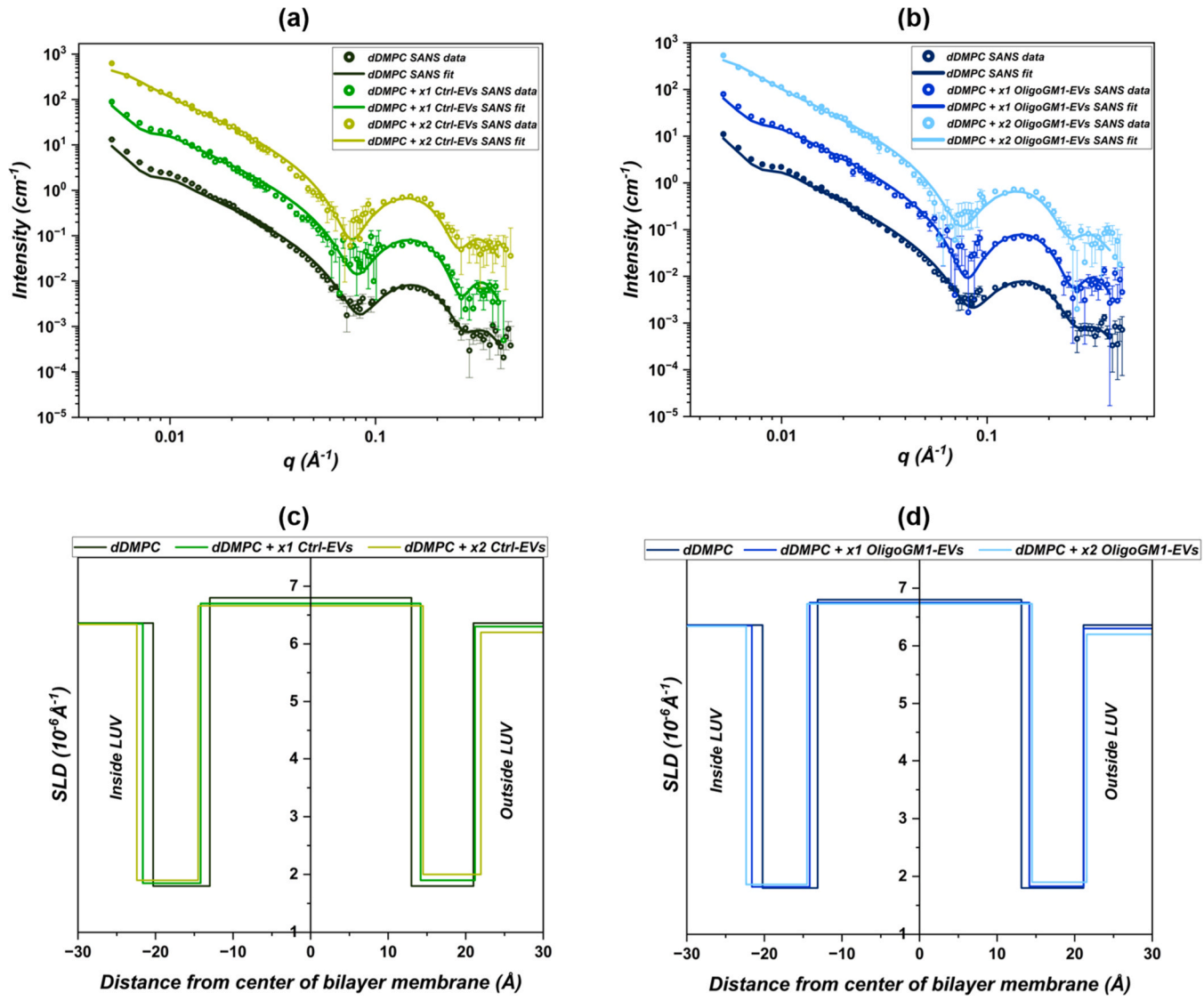


Fig. 7. SANS data points and corresponding best fits for d_{54}DMPC LUVs at 37 °C in PBS prepared in 100% D_2O, before and after interaction with increasing volumes (x1, x2) of (a) Ctrl-EVs and (b) OligoGM1-EVs. For better visibility, the d_{54}DMPC + x1 Ctrl-EVs dataset and fit (vivid green in a) and the d_{54}DMPC + x1 OligoGM1-EVs dataset and fit (vivid blue in b) were shifted vertically by a factor of 10^1. The d_{54}DMPC + x2 Ctrl-EVs dataset and fit (pale green in a) and the d_{54}DMPC + x2 OligoGM1-EVs dataset and fit (pale blue in b) were shifted vertically by a factor of 10^2. The original non-offset SANS profiles are shown in Fig. S16. Corresponding SLD profiles of d_{54}DMPC LUVs before and after interaction with increasing volumes of (c) Ctrl-EVs (in shades of green) and (d) OligoGM1-EVs (in shades of blue).

their own EV-derived protiated lipids (Fig. 8**c,d** and SI, Fig. S17) consistent with an accelerated target membrane lipid disruption within the probed interfacial region. OligoGM1-EVs extracted $< 5 \pm 1\%$ in the same window and displayed a slow, gradual lipid exchange profile over 45 min (Fig. 8**d** and SI, Fig. S17). These data further support the hypothesis that OligoGM1-EVs preserve membrane integrity far better than Ctrl-EVs during early interaction stages.

Simultaneously, the rise in C–H stretching bands (Fig. 8**c,d**) revealed the insertion of protiated EV lipids into the SLB, marking direct lipid exchange between the two bilayers. This process reflects EV–membrane mixing at the molecular level, consistent with lipid exchange within the probed interfacial region.

The C═O stretching region (1900–1500 cm^{-1}) likewise displayed changes indicative of local perturbation in headgroup environments, including reduced ester carbonyl absorbance and increased aromatic C═C contributions (Fig. 8**e,f**).

Quantitative integration of the C–D and C–H bands over 45 min (SI Fig. S18) showed distinct kinetic behaviours: OligoGM1-EVs exhibited a controlled and sustained lipid exchange profile, with final SLB lipid loss of only $6 \pm 2\%$. In contrast, Ctrl-EVs caused substantial depletion ($20 \pm 1\%$), consistent with aggressive lipid extraction and membrane destabilization. With an overall average lipid exchange efficiency of $11 \pm 1\%$ compared to only $5 \pm 1\%$ for Ctrl-EVs, OligoGM1-EVs indicate to be significantly less membrane-disruptive. Specifically, they were twice as efficient at mediating a balanced lipid exchange, utilizing their own EV-derived lipids to offset the lipids lost from the target bilayer.

3.2.5. Protein insertions from the EVs into DMPC and raft d_{54}DMPC/SM/Chol SLBs by Neutron Reflectometry (NR)

Since protein related absorbance peaks were out of the measured IR spectral range, and to resolve the transverse structural changes occurring within SLBs upon interaction with EVs, neutron reflectometry (NR) measurements were performed. NR provides angstrom-scale information on layer thickness, solvent penetration, and the scattering length density (SLD) profile across bilayer surface normal. By exploiting contrast variation in H_2O and D_2O, NR enables sensitive detection of protiated EV-derived components inserted into the deuterated or protiated model membranes. All NR measurements have been performed at

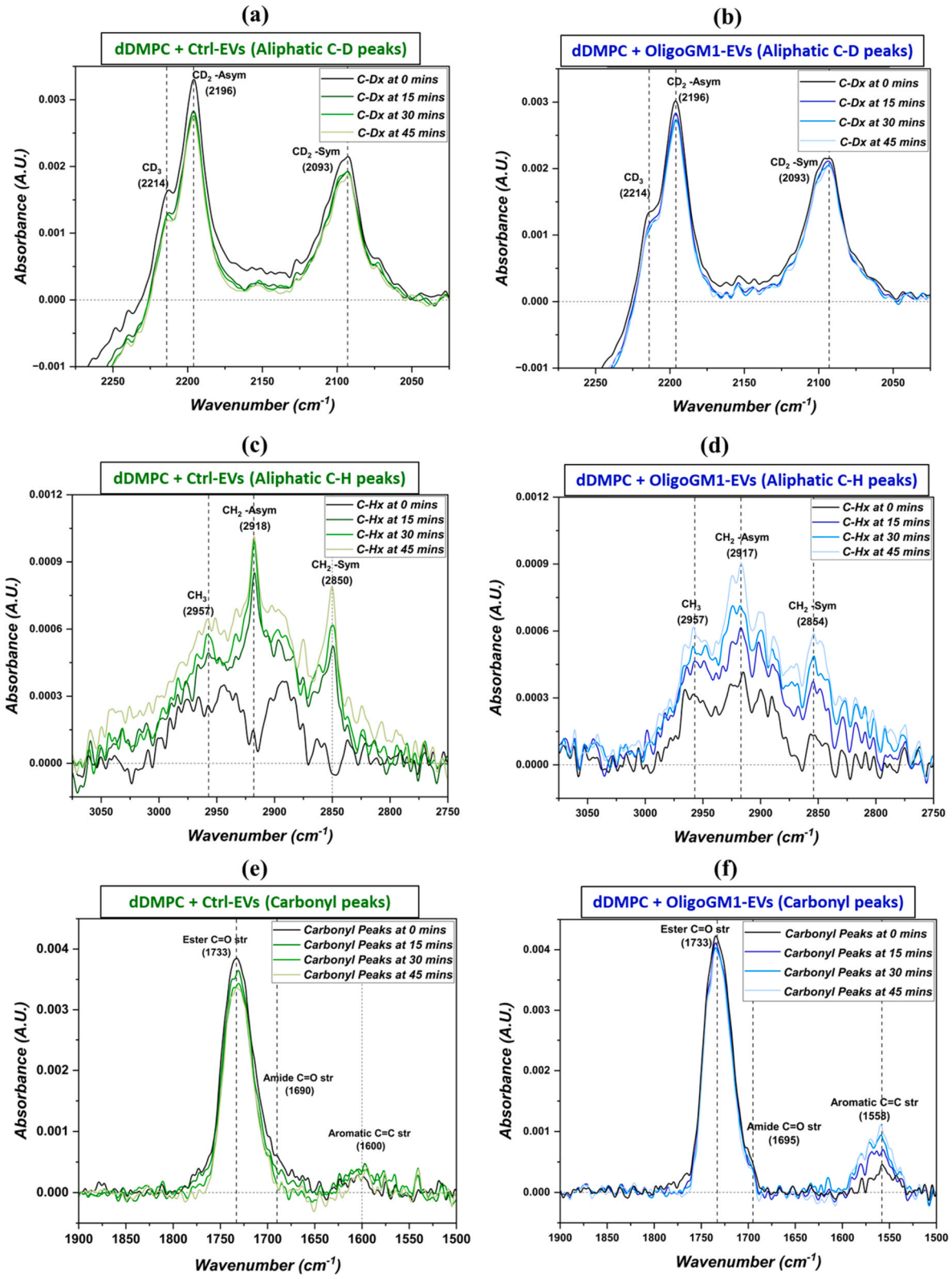


Fig. 8. Excerpts of the ATR-FTIR spectra during the interaction of EVs with the d_{54}DMPC SLB in 150 mM NaCl. Spectral region of 2275–2025 cm^{-1} showing the decrease of the aliphatic C-Dx peaks of the d_{54}DMPC SLB tail region upon interaction with: (a) Ctrl-EVs; (b) OligoGM1-EVs. Spectral region of 3075–2750 cm^{-1} showing the increase of the aliphatic C-Hx peaks due to lipidic insertions from EVs into the d_{54}DMPC SLB upon interaction with: (c) Ctrl-EVs; (d) OligoGM1-EVs. Spectral region of 1900–1500 cm^{-1} showing the evolution of the carbonyl peak corresponding to the C═O stretching vibration of the neck region of the d_{54}DMPC SLB upon interaction with: (e) Ctrl-EVs; (f) OligoGM1-EVs. Temperature= 37 °C. Data are representative of repeated independent experiments with pooled EV material. Values in the main text are reported as mean ± variability across repeated independent ATR-FTIR experiments performed with pooled EV material under identical conditions; the reported uncertainty reflects run-to-run variability.

the physiological temperature of 37 °C. Neutron reflectometry data were modelled in anaklasis software, by a stratified (layer-based) SLD representation of the SLB. Bilayer thickness is obtained from the fitted layer thicknesses, while solvent penetration in the hydrophobic region is quantified from the fitted tail-layer parameters as a solvent fraction/contrast contribution within the layer model. NR is laterally averaged over the illuminated footprint; discrete protrusions/patches are not uniquely resolved unless they contribute significantly to the average coverage. Therefore, NR-derived parameters are used to describe average changes in thickness/contrast/solvent penetration across the SLB profile under the stated model. Layer-specific solvent volume fractions (i.e., hydration/solvation levels), average changes in thickness and SLD values are explicitly reported in the SI tables (S8–11) for each layer, providing the volume-fraction–type information requested within our modelling framework.

i) DMPC SLBs (Protiated Model Membrane)

DMPC SLBs were used to selectively detect protein insertion, as the hydrophobic tail region of DMPC (SLD ≈ –0.39 × 10^{-6} Å^{-2}) provides

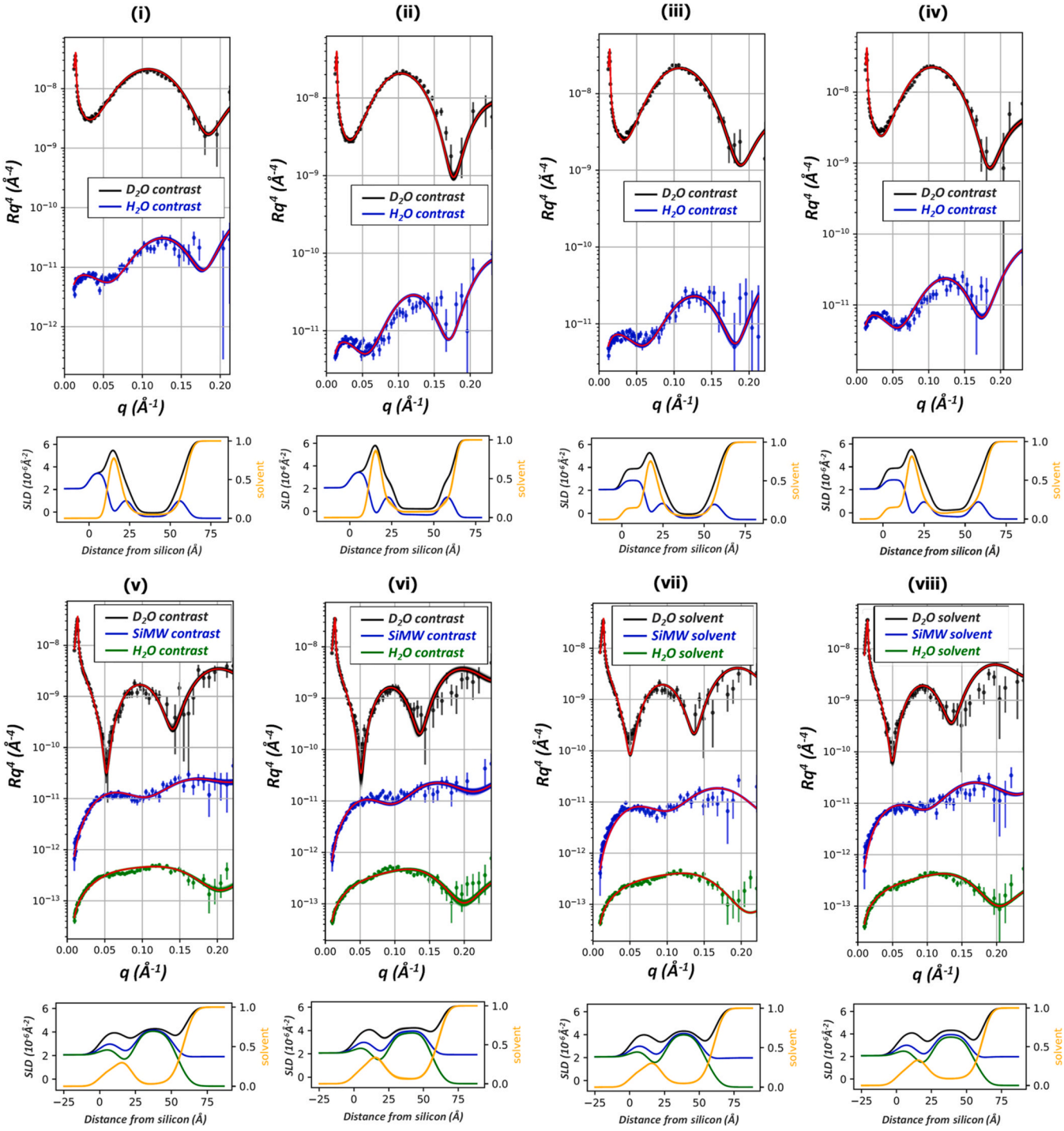


Fig. 9. Best fits panels of the NR reflectivity curves (above) and their corresponding SLD profiles (below) for the SLBs of: (i) DMPC and (ii) DMPC + Ctrl-EVs, then (iii) DMPC and (iv) DMPC + OligoGM1-EVs, all in D_2O and H_2O solvents at 37 °C. Then (v) dRaft and (vi) dRaft + Ctrl-EVs, then (vii) dRaft and (viii) dRaft + OligoGM1-EVs, all in D_2O, SiMW and H_2O solvents at 37 °C. The H_2O reflectivity curves are shifted down on the vertical axis each by 10^{-3}, for better clarity. In the SLD profiles, colours denote black in D_2O, blue in SiMW and H_2O in green, consistent with the ordering of panels (i–viii) described in the caption.

strong contrast against EV-associated proteins (SLD ≈ 2.5 × 10^{-6} Å^{-2}) while masking eventual lipid insertion. NR measurements revealed (Fig. 9 **i-iv**; SI Tables S8,9) that both EV types induced modest increases in bilayer thickness (2 ± 1 Å for Ctrl-EVs; 3 ± 1 Å for OligoGM1-EVs) and enhanced relative volume of solvent penetration into the full SLB bilayer (up to 9 ± 3% in the outer head groups). These changes confirm that EV components can penetrate both leaflets of the DMPC bilayer.

However, quantitative SLD differences revealed markedly distinct protein insertion behaviours. Ctrl-EVs increased the overall SLD of the DMPC tail region from –0.39 × 10^{-6} Å^{-2} to –0.30 ± 0.05 × 10^{-6} Å^{-2}, whereas OligoGM1-EVs induced only a slight increase to –0.35 ± 0.05 × 10^{-6} Å^{-2}. Based on these shifts, protein volume insertion was estimated at ~5% for Ctrl-EVs and ~2% for OligoGM1-EVs. This reduced incorporation is consistent with their reduced ability to exchange molecules from OligoGM1-EVs to target bilayers observed by AFM and SANS.

ii) dRaft SLBs (Deuterated Raft Model Membrane)

We subsequently evaluated EV interactions with the more biologically relevant, liquid-ordered membrane, composed of deuterated d_{54}DMPC, SM, and cholesterol (i.e. dRaft SLB described in [45]). In this model, both protein and lipid insertions from EVs lead to a decrease in the SLD of the tail region (SLD ≈ 4.25 × 10^{-6} Å^{-2}), enabling detection of multiple molecular processes (Fig. 9**v-viii**; SI Tables S10,11).

Upon incubation, both EV types induced an increased averaged solvent penetration across the full bilayer (7 ± 3% for Ctrl-EVs; 3 ± 3% for OligoGM1-EVs). The tails averaged SLD decreased to 4.13 × 10^{-6} Å^{-2} in both cases, indicating insertion of protiated material, but the headgroup region responded differently to the two EV types. Ctrl-EVs raised the outer-headgroup SLD from 1.7 × 10^{-6} Å^{-2} to 1.95 ± 0.05 × 10^{-6} Å^{-2}, whereas OligoGM1-EVs induced no such increase.

Collectively, these results support the hypothesis that Ctrl-EVs mediate greater protein insertion into both simple and raft-like membranes compared to OligoGM1-EVs, strongly providing convergent support to the conclusions drawn from AFM, ATR-FTIR, and SANS. Hence, OligoGM1-EVs interact with SLBs in a more regulated, less invasive manner, causing minimal structural perturbation while maintaining selectivity for ordered membrane domains.

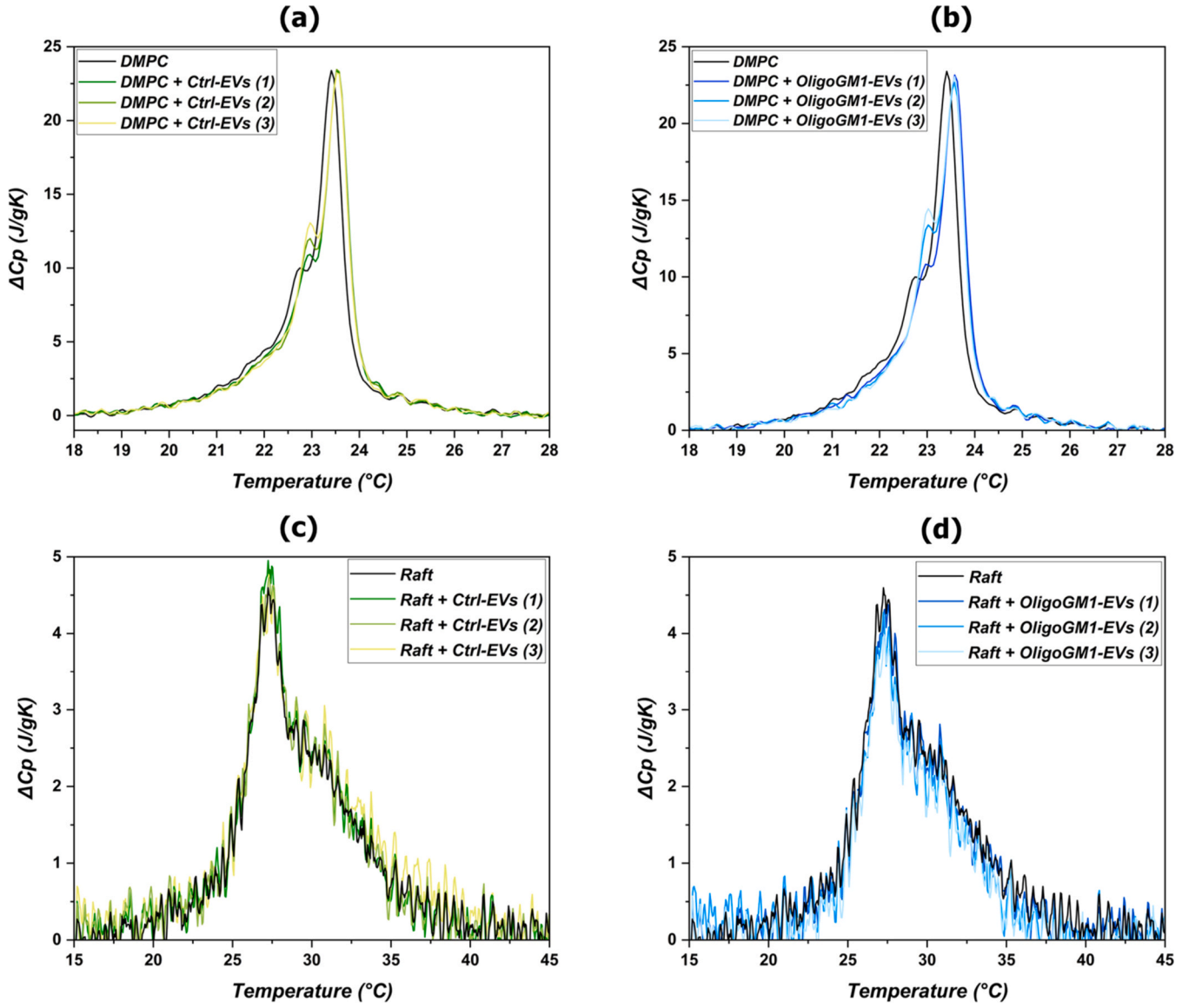


Fig. 10. A comparison between the DSC thermograms (ΔCp) of the DMPC and Raft LUVs after interacting with increasing equal volumes of both types of EVs. (a) thermograms of DMPC LUVs upon interacting with increasing volumes of Ctrl-EVs. (b) thermograms of DMPC LUVs upon interacting with increasing volumes of OligoGM1-EVs. (c) thermograms of Raft LUVs upon interacting with increasing volumes of Ctrl-EVs. (d) thermograms of Raft LUVs upon interacting with increasing volumes of OligoGM1-EVs. Scan rate 1°C/3 min, in cooling mode.

3.2.6. Thermotropic behaviour of LUVs upon EVs Interaction (DSC)

Differential scanning calorimetry (DSC) was used to probe how EV interaction modifies the thermotropic behaviour of target model membranes, providing insight into EV-driven alterations in lipid packing and phase transitions, using both DMPC LUVs and raft-like mixture (DMPC: SM:Chol, 2:1:0.15) LUVs. Data shown in Fig. 10**a,b** and in SI Figs. S19–22 are reported as excess Cp (ΔCp) registered during the phase transition.

The thermogram of bare DMPC LUVs was characterized by two peaks, one at lower T corresponding to lipids in the inner (concave) leaflet, the other at higher-temperature transition associated with the outer (convex) leaflet (Fig. S20). Upon addition of increasing amounts of either Ctrl-EVs and OligoGM1-EVs, both transitions shifted slightly to higher temperatures, indicating that EV interaction stabilizes lipid packing and increases the energetic cost of the gel–fluid transition. In both cases, the inner leaflet associated peak shifted more sensibly than the outer leaflet one (Fig. S21,22).

On the other hand, the raft-mimicking membrane exhibited more complex thermograms due to phase coexistence and the presence of SM/Chol-enriched ordered domains (Fig. 10**c,d**). Upon EV addition, only subtle changes were detectable, reflecting the intrinsic stability and lower fluidity of raft-like bilayers.

The total transition enthalpy (ΔH) of DMPC LUVs increased after both Ctrl-EVs and OligoGM1-EVs addition **(**SI Table S12 and Fig. S23**)**. Lorentzian deconvolution [16,17] of the thermograms confirmed that lipids in the inner leaflet experienced the greatest enthalpy increase (+18% for Ctrl-EVs and +27% for OligoGM1-EVs). The upward shift in melting temperature is consistent with EV-derived components enhancing effective chain ordering and cooperative packing within the DMPC bilayer, thereby increasing the energetic cost of the gel–fluid transition. This suggests that OligoGM1-EVs induce a stronger ordering effect to the target bilayer [16,17,70].

Instead, in raft-mimicking LUVs, OligoGM1-EVs induced a modest decrease in the transition enthalpy, in particularly corresponding to the higher temperature peak, associated with SM- and Chol-rich domains, suggesting that OligoGM1-EVs differentially affect the ordered component of the raft-like membrane. This finding is qualitatively consistent with the frequent association of OligoGM1-EV interaction sites with L_o/L_d boundary regions observed by AFM.

4. Discussion

The central premise of this work is that OligoGM1, administered to Neuro2a cells prior to EV isolation, modulates endocytic trafficking and EV biogenesis, thereby reshaping the molecular organization of the released vesicles. Our multi-technique characterization shows that Ctrl- and OligoGM1-derived EVs remain broadly comparable by bulk properties (size/concentration), yet display consistent and reproducible differences at the level of composition and membrane structure. This supports the view that EV populations are intrinsically heterogeneous, and that biologically relevant differences may only emerge through the integration of orthogonal descriptors rather than single readouts.

ATR-FTIR provides a global spectroscopic protein-to-lipid balance, while SAXS adds structural information on bilayer thickness and contrast. Taken together, the reduced FTIR protein-to-lipid spectroscopic ratio and the SAXS-derived bilayer contrast/SLD changes, consistent with increased protein contribution within the membrane model, suggest a redistribution of protein content, in which the relative contribution of membrane-associated proteins increases while the overall protein-to-lipid balance decreases—implying a reduced relative contribution from luminal/soluble proteins. Importantly, SAXS alone cannot uniquely identify the molecular origin of the membrane-thickness increase. We therefore interpret these changes as model-dependent structural and contrast variations that are consistent with a redistribution of lipid/protein contributions only when considered together with the complementary ATR-FTIR and neutron-based readouts. This rearrangement is consistent with treatment-driven changes in endosomal/raft-associated EV biogenesis and is expected to influence how EVs interface with recipient membranes. We therefore probed EV interactions with model membranes. AFM on phase-separating raft-like SLBs suggests that membrane lateral organization influences the spatial pattern of EV engagement. OligoGM1-EV interaction sites were frequently observed in association with L_o/L_d boundaries, whereas Ctrl-EVs interacted more broadly across the heterogeneous bilayer. Because the phase identity underneath an interacting EV cannot be unambiguously reconstructed from post-interaction topography, we interpret this difference as a qualitative boundary-associated interaction fingerprint rather than as a quantitatively established phase preference. Such an association is nevertheless physically plausible, as L_o/L_d boundaries present local packing and elastic discontinuities that can favour nanoscale interactions with membrane-bound objects. Temperature-dependent measurements were performed for DMPC-based LUV systems because DMPC exhibits a gel–fluid transition near ~24 °C, making temperature a key determinant of bilayer mechanical response and of whether interaction signatures are detectable by DLS. By contrast, AFM experiments were conducted on raft-like DOPC:SM:Chol SLBs, which are already in a fluid regime at room temperature and do not undergo a comparable phase transition between 25 °C and 37 °C. Room-temperature AFM provides improved experimental stability for time-lapse imaging in liquid (reduced drift/evaporation effects) while capturing the nanoscale docking and remodelling patterns that are central to our comparative analysis.

Time-lapse AFM further shows that Ctrl-EVs induce more extensive morphological remodelling over time (higher roughness and broader disrupted area), whereas OligoGM1-EVs display slower and spatially confined remodelling, indicating a more localized remodelling footprint on heterogeneous membranes.

Component-resolved and depth-sensitive readouts (ATR-FTIR on isotopically labelled SLBs; SANS on deuterated LUVs; NR with contrast variation) provide a consistent picture for how Ctrl- and OligoGM1-EVs differ in the extent and depth of material exchange with target membranes.

ATR-FTIR on deuterated SLBs quantifies net lipid depletion from the supported bilayer and the concomitant appearance of EV-derived protiated lipid signal in the probed interfacial region; Ctrl-EVs show markedly faster and larger net lipid depletion than OligoGM1-EVs, supporting a more efficient interfacial lipid exchange rate for OligoGM1-EVs.

SANS on deuterated LUVs complements these findings by providing ensemble-averaged, depth-resolved constraints on the bilayer SLD profile. The fitted SLD changes are consistent with the incorporation of EV-derived (protiated) material within the LUV bilayer, and the relative magnitude of these changes differs between Ctrl- and OligoGM1-EVs; the dose-dependent trends and the consistent directionality of higher protein insertions into the target membranes from the Ctrl-EVs than the OligoGM1-EVs supplement the results of the lipid exchange rates from the ATR-FTIR kinetics. In line with AFM and ATR-FTIR, SANS results support a higher overall ability of Ctrl-EVs for protein incorporation into the target membrane, whereas OligoGM1-EVs exhibit reduced depth-resolved incorporation/mixing under the tested conditions.

NR adds a complementary constraint on planar SLBs, where contrast variation permits estimation of average thickness, solvent penetration, and changes in SLD consistent with incorporation of EV-derived material into specific bilayer regions within the layer model. As a laterally averaged method, NR does not resolve isolated protrusions/patches; however, it is uniquely informative about depth-dependent contrast changes across the membrane profile. In both simple (DMPC) and raft-like (dRaft) SLBs, the relative insertion/contrast changes are larger for Ctrl-EVs than for OligoGM1-EVs, reinforcing the conclusion that OligoGM1 treatment reduces the degree of EV-derived proteic material incorporation into target bilayers under the tested conditions.

Across ATR-FTIR, SANS and NR, the most coherent mechanistic

statement is therefore a treatment-dependent shift in the extent and kinetics of material exchange and bilayer incorporation: Ctrl-EVs promote more rapid net lipid depletion and a greater overall extent of protein incorporation across the membrane depth, whereas OligoGM1-EVs produce less extensive membrane remodelling and show a qualitatively distinct, boundary-associated spatial interaction pattern on heterogeneous SLBs. We also investigated how EV interaction affects membrane thermodynamics. Hence for that, DSC provides an energetics-based, ensemble readout of how EV exposure perturbs target membrane lipid packing. For DMPC LUVs, both EV types shift the transition temperatures upward and increase the transition enthalpy, with a stronger response for the less packed components. The upward T_m shift is consistent with EV-derived components enhancing effective chain ordering and cooperative packing within the DMPC bilayer, increasing the energetic cost of the lipids gel–fluid transition. These shifts do not uniquely specify the molecular species responsible (lipids, sterols, membrane proteins), but they support the broader picture that EV–membrane coupling can stabilize certain packing interactions even when some incorporation/transfer occurs.

In raft-mimicking LUVs, the thermograms are more complex and changes are subtle, consistent with the intrinsic stability of SM/Chol-enriched ordered regions; the modest reduction in enthalpy associated with the higher-temperature component upon OligoGM1-EV exposure is compatible with preferential engagement with ordered domains, consistent with AFM docking selectivity.

Overall, DSC supports the view that OligoGM1-EVs perturb membrane packing less strongly than Ctrl-EVs while maintaining a selective interaction fingerprint; these controlled interfacial regimes may be relevant for future studies connecting membrane-level EV fingerprints to cell-facing endpoints in neurodegenerative models [71].

Taken together, the data support a working hypothesis in which OligoGM1-driven modulation of cellular trafficking/biogenesis produces EVs with altered lipid–protein architecture and membrane organization, which in turn biases EV–membrane coupling toward (i) L_o/L_d boundaries selective docking on heterogeneous membranes and (ii) reduced net lipid depletion and markedly less invasive depth-resolved protein incorporation into target bilayers. This defines an interaction regime that is selective and comparatively low-disruption, relative to Ctrl-EVs, within the sensitivity of the employed biophysical assays.

At the same time, several scope limitations should be made explicit. (i) The model membranes (DMPC-based and raft-like mixtures) are simpler than natural membranes; their value here is to enable component-resolved and depth-resolved inference. (ii) Some large-scale facilities experiments rely on pooled material and fit-derived uncertainties; the reported parameters are therefore ensemble descriptors and should not be over-interpreted as unique microscopic pathways. (iii) Differential ultracentrifugation combined with filtration provides EV-enriched preparations rather than molecularly pure EV isolates [44]; therefore, associated or co-isolated biomolecular components may contribute to the effective corona and interfacial behaviour of the EV preparations. However, because Ctrl- and OligoGM1-EVs were isolated using the same workflow, the comparative trends between the two conditions remain internally controlled. (iv) The present study does not directly measure EV uptake, cargo delivery, or biological activity in recipient cells; therefore, the observed differences should be interpreted as membrane-level interaction fingerprints rather than direct evidence of altered EV-mediated communication in vivo. (v) The present study was conducted using N2a cells as a controlled neuronal-like model. Accordingly, the observed OligoGM1-dependent differences in EV composition, membrane structure, and interfacial behaviour should not be generalized to neuronal EV biology without validation in primary neurons or additional neuronal models. Future studies are required to determine whether these features are conserved in more physiologically representative neuronal systems.

Beyond the specific neuronal model, the key advance for colloid and interface science is the component-resolved, multi-technique framework that links EV compositional/structural fingerprints to membrane-level interaction readouts across orthogonal methods. This workflow is generalizable to EVs from other sources and to more complex biomimetic membranes, enabling systematic exploration of how membrane composition, lateral organization, and domain structure regulate material exchange and remodelling. Future work will connect these membrane-level fingerprints to cell-facing endpoints. Future work will address the dose dependence of OligoGM1 effects and include structurally related oligosaccharide controls (e.g., OligoGM2, OligoGM3) to further validate the molecular specificity of the observed EV reprogramming.

5. Conclusion

This study indicates that the GM1-derived oligosaccharide OligoGM1, administered to N2a cells before extracellular vesicle (EV) isolation, acts as a regulator of the interfacial behaviour of the secreted EVs, with limited effects on bulk size and concentration but measurable consequences on membrane architecture and EV–bilayer interaction pathways. By implementing our recent and successful strategy [13–15,17,45], we integrated complementary techniques spanning composition, membrane structure, nanoscale morphology, and depth-resolved interfacial processes, to establish a coherent structure–function picture in which subtle changes in EV molecular organization translate into distinct interaction regimes with model membranes. Spectroscopic and scattering analyses indicate that EVs derived from OligoGM1-treated cells display a shifted protein/lipid balance and a modified membrane organization, consistent with thicker bilayers and a redistribution of protein contributions between membrane-associated and soluble fractions.

Given the fundamental importance of EV–membrane interactions for cargo delivery and functional activity [18], we also tested EV coupling to complex model membranes. Nanoscale imaging on phase-separating supported lipid bilayers indicates a qualitatively distinct spatial pattern of interaction for OligoGM1-EVs, with docking events frequently observed near L_o/L_d boundaries, whereas Ctrl-EVs interact more broadly and induce more extensive morphological remodelling over time. Depth-sensitive neutron approaches provide convergent support for this distinction by indicating a lower degree of EV-derived proteic material incorporation into target bilayers for OligoGM1-EVs relative to Ctrl-EVs, while time-resolved ATR-FTIR on isotopically labelled supported bilayers reveals markedly reduced net lipid depletion and more efficient lipid-exchange kinetics for OligoGM1-EVs.

Together, these convergent observations support the working hypothesis that OligoGM1-driven modulation of cellular trafficking and EV biogenesis [20,27,33,37,38,41,42,43] yields vesicles with altered lipid–protein architecture, which in turn biases EV–membrane engagement toward selective, comparatively low-disruption interaction modes.

The observed differences in EV–membrane interactions underscore the importance of nanoscale membrane organization in governing EV function: small variations in lipid–protein architecture, undetectable by bulk metrics alone [8,10], can translate into pronounced differences in membrane penetration, material transfer, and domain specificity.

From a broader perspective, these findings expand the functional scope of OligoGM1 beyond its established role in neurotrophic signalling [20,27,33,37,38,41,42,43]. By reprogramming the molecular and biophysical properties of EVs, OligoGM1 may indirectly modulate EV-mediated communication, a process increasingly implicated in both physiological neuronal signalling and the spread of neurodegenerative pathology. The generation of EVs with reduced membrane engagement and regulated molecular exchange may therefore represent a protective or homeostatic mechanism in the nervous system.

Beyond the specific biological system, the main advance for colloid and interface science is the component-resolved, multi-technique framework introduced here, which reduces ambiguity in interpreting EV–membrane coupling by linking compositional/structural signatures

to interface-level outcomes across orthogonal readouts, rather than relying on a single phenomenological descriptor. In this perspective, the workflow provides a general strategy to establish quantitative structure–interaction relationships for biologically relevant nanocolloids and can be extended to EVs from other sources and to more complex biomimetic membranes, enabling systematic investigation of how membrane composition, lateral organization, and domain structure shape material exchange and bilayer remodelling.

Future work will translate these membrane-level determinants to cell-facing endpoints; to determine how selective, low-disruption interfacial regimes influence uptake routes [18], signalling and cargo delivery in physiologically relevant contexts.

Funding

Sally Helmy was funded by a full PhD scholarship (mission 2019/2020) from the cultural affairs and missions sector of the Ministry of Higher Education in Egypt. This research was funded by Mizutani Foundation for Glycoscience 27th Research Grant, grant number 200045 to E.C, by Italian Ministry of University and Research (MUR), PRIN2020 project n. 2020MHL8S9 "MITHOS" to V.R, "Next Generation EU Missione 4 Componente 1", for the project n. G53D2300330000, CUP G53D23003300001 to V.R., by "Next Generation EU Missione 4 Componente 1", for the project n. P2022J2ZC2, CUP G53D23007030001 to V.R. and P.P, by the European Union - NextGenerationEU, Mission 4, Component 2, under the Italian Ministry of University and Research (MUR) National Innovation Ecosystem grant ECS00000041 - VITALITY - CUP B43C22000470005 to P.P.

CRediT authorship contribution statement

Sally Helmy: Writing – review & editing, Writing – original draft, Methodology, Investigation, Formal analysis, Data curation. **Giulia Lunghi:** Writing – review & editing, Methodology, Investigation. **Alexandros Koutsioubas:** Writing – review & editing, Methodology, Investigation. **Stephen C.L. Hall:** Writing – review & editing, Methodology, Investigation. **Miriam Grava:** Writing – review & editing, Methodology, Investigation. **Hendrik Vondracek:** Writing – review & editing, Methodology, Investigation. **László Almásy:** Writing – review & editing, Methodology, Investigation. **László Bottyán:** Writing – review & editing, Methodology, Investigation. **Martin Rosenthal:** Writing – review & editing, Methodology, Investigation. **Maria Fazzari:** Writing – review & editing, Methodology, Investigation. **Laura Mauri:** Writing – review & editing, Methodology, Investigation. **Maria Grazia Ciampa:** Writing – review & editing, Methodology, Investigation. **Chiara Adriana Elia:** Writing – review & editing, Methodology, Investigation. **Elena Monica Borroni:** Writing – review & editing, Methodology, Investigation. **Sandro Sonnino:** Writing – review & editing, Methodology, Investigation. **Pietro Parisse:** Writing – review & editing, Writing – original draft, Methodology, Investigation, Data curation. **Paola Brocca:** Writing – review & editing, Writing – original draft, Supervision, Methodology, Investigation. **Elena Chiricozzi:** Writing – review & editing, Writing – original draft, Methodology, Investigation. **Loredana Casalis:** Writing – review & editing, Writing – original draft, Supervision, Methodology, Investigation, Funding acquisition, Data curation, Conceptualization. **Valeria Rondelli:** Writing – review & editing, Writing – original draft, Supervision, Project administration, Methodology, Funding acquisition, Conceptualization.

Declaration of Competing Interest

The authors declare the following financial interests/personal relationships which may be considered as potential competing interests: Sally Helmy reports financial support was provided by cultural affairs and missions sector of the Ministry of Higher Education in Egypt. Elena Chiricozzi reports financial support was provided by Mizutani Foundation for Glycoscience. Valeria Rondelli reports financial support was provided by Italian Ministry of University and Research. Valeria Rondelli reports financial support was provided by Next Generation EU. Pietro Parisse reports financial support was provided by Next Generation EU. Luca Puricelli reports financial support was provided by Next Generation EU. Loredana Casalis reports financial support was provided by Next Generation EU. If there are other authors, they declare that they have no known competing financial interests or personal relationships that could have appeared to influence the work reported in this paper.

Acknowledgments

This work benefited from the use of the Offspec vertical neutron reflectometer beamtimes; https://doi.org/10.5286/ISIS.E.RB2210183 and https://doi.org/10.5286/ISIS.E.RB2210198 at the ISIS Neutron and Muon Source, Oxfordshire, UK. This work benefited from the use of the anaklasis; open-source Python3 scripts provided by Alexandros Koutsioubas. This work benefited from the use of the ID02 and BM26 beamlines at the European Synchrotron Radiation Facility (ESRF) in Grenoble, France. This work benefited from the use of the neutron facilities at Budapest Neutron Center. This work benefited from the use of the SasView application, http://www.sasview.org/, originally developed under NSF award DMR-0520547. SasView contains code developed with funding from the European Union's Horizon 2020 research and innovation programme under the SINE2020 project, grant agreement No 654000. This work benefited from the use of the SISSI-Bio offline facility at ELETTRA Sincrotrone in Trieste (Italy).

Appendix A. Supporting information

Supplementary data associated with this article can be found in the online version at:doi:10.1016/j.colsurfb.2026.116258

Data availability

Data will be made available on request.

References

[1] C. Théry, K.W. Witwer, E. Aikawa, M.J. Alcaraz, J.D. Anderson, R. Andriantsitohaina, A. Antoniou, T. Arab, F. Archer, G.K. Atkin-Smith, D.C. Ayre, J. Bach, D. Bachurski, H. Baharvand, L. Balaj, S. Baldacchino, N.N. Bauer, A. A. Baxter, M. Bebawy, C. Beckham, A. Bedina Zavec, A. Benmoussa, A.C. Berardi, P. Bergese, E. Bielska, C. Blenkiron, S. Bobis-Wozowicz, E. Boilard, W. Boireau, A. Bongiovanni, F.E. Borràs, S. Bosch, C.M. Boulanger, X. Breakefield, A.M. Breglio, M.Á. Brennan, D.R. Brigstock, A. Brisson, M.L. Broekman, J.F. Bromberg, P. Bryl-Górecka, S. Buch, A.H. Buck, D. Burger, S. Busatto, D. Buschmann, B. Bussolati, E. I. Buzás, J.B. Byrd, G. Camussi, D.R. Carter, S. Caruso, L.W. Chamley, Y. Chang, C. Chen, L. Cheng, A.R. Chin, A. Clayton, S.P. Clerici, A. Cocks, E. Cocucci, R. J. Coffey, A. Cordeiro-da-Silva, Y. Couch, F.A. Coumans, B. Coyle, R. Crescitelli, M. F. Criado, C. D'Souza-Schorey, S. Das, A. Datta Chaudhuri, P. de Candia, E.F. De Santana, O. De Wever, H.A. del Portillo, T. Demaret, S. Deville, A. Devitt, B. Dhondt, D. Di Vizio, L.C. Dieterich, V. Dolo, A.P. Dominguez Rubio, M. Dominici, M.R. Dourado, T.A. Driedonks, F.V. Duarte, H.M. Duncan, R. M. Eichenberger, K. Ekström, S. El Andaloussi, C. Elie-Caille, U. Erdbrügger, J. M. Falcón-Pérez, F. Fatima, J.E. Fish, M. Flores-Bellver, A. Försönits, A. Frelet-Barrand, F. Fricke, G. Fuhrmann, S. Gabrielsson, A. Gámez-Valero, C. Gardiner, K. Gärtner, R. Gaudin, Y.S. Gho, B. Giebel, C. Gilbert, M. Gimona, I. Giusti, D. C. Goberdhan, A. Görgens, S.M. Gorski, D.W. Greening, J.C. Gross, A. Gualerzi, G. N. Gupta, D. Gustafson, A. Handberg, R.A. Haraszti, P. Harrison, H. Hegyesi, A. Hendrix, A.F. Hill, F.H. Hochberg, K.F. Hoffmann, B. Holder, H. Holthofer, B. Hosseinkhani, G. Hu, Y. Huang, V. Huber, S. Hunt, A.G. Ibrahim, T. Ikezu, J. M. Inal, M. Isin, A. Ivanova, H.K. Jackson, S. Jacobsen, S.M. Jay, M. Jayachandran, G. Jenster, L. Jiang, S.M. Johnson, J.C. Jones, A. Jong, T. Jovanovic-Talisman, S. Jung, R. Kalluri, S. Kano, S. Kaur, Y. Kawamura, E.T. Keller, D. Khamari, E. Khomyakova, A. Khvorova, P. Kierulf, K.P. Kim, T. Kislinger, M. Klingeborn, D. J. Klinke, M. Kornek, M.M. Kosanović, Á.F. Kovács, E. Krämer-Albers, S. Krasemann, M. Krause, I.V. Kurochkin, G.D. Kusuma, S. Kuypers, S. Laitinen, S. M. Langevin, L.R. Languino, J. Lannigan, C. Lässer, L.C. Laurent, G. Lavieu, E. Lázaro-Ibáñez, S. Le Lay, M. Lee, D.S. Lemos, M. Lenassi, A. Leszczynska, I.T. Li, K. Liao, S.F. Libregts, E. Ligeti, R. Lim, A. Linë, K. Linnemannstöns, A. Llorente, C. A. Lombard, M.J. Lorenowicz, Á.M. Lörincz, J. Lötvall, J. Lovett, M.C. Lowry, X. Loyer, Q. Lu, B. Lukomska, T.R. Lunavat, S.L. Maas, H. Malhi, A. Marcilla, J. Mariani, J. Mariscal, E.S. Martens-Uzunova, L. Martin-Jaular, M.C. Martinez, V.

R. Martins, M. Mathieu, S. Mathivanan, M. Maugeri, L.K. McGinnis, M.J. McVey, D. G. Meckes, K.L. Meehan, I. Mertens, V.R. Minciacchi, A. Möller, M. Møller Jørgensen, A. Morales-Kastresana, J. Morhayim, F. Mullier, M. Muraca, L. Musante, V. Mussack, D.C. Muth, K.H. Myburgh, T. Najrana, M. Nawaz, I. Nazarenko, P. Nejsum, C. Neri, R. Nieuwland, L. Nimrichter, J.P. Nolan, E.N. Nolte-'t Hoen, N. Noren Hooten, L. O'Driscoll, T. O'Grady, A. O'Loghlen, T. Ochiya, M. Olivier, A. Ortiz, X. Osteikoetxea, O. Østergaard, M. Ostrowski, J. Park, D.M. Pegtel, H. Peinado, F. Perut, M.W. Pfaffl, D.G. Phinney, B.C. Pieters, R.C. Pink, D. S. Pisetsky, E. Pogge von Strandmann, I. Polakovicova, I.K. Poon, B.H. Powell, I. Prada, L. Pulliam, P. Quesenberry, A. Radeghieri, R.L. Raffai, S. Raimondo, J. Rak, M.I. Ramirez, G. Raposo, M.S. Rayyan, N. Regev-Rudzki, F.L. Ricklefs, P. D. Robbins, D.D. Roberts, S.C. Rodrigues, E. Rohde, S. Rome, K.M. Rouschop, A. Rughetti, A.E. Russell, P. Saá, S. Sahoo, E. Salas-Huenuleo, C. Sánchez, J. A. Saugstad, M.J. Saul, R.M. Schiffelers, R. Schneider, T.H. Schøyen, A. Scott, E. Shahaj, S. Sharma, O. Shatnyeva, F. Shekari, G.V. Shelke, A.K. Shetty, K. Shiba, P.R. Siljander, A.M. Silva, A. Skowronek, O.L. Snyder, R.P. Soares, B.W. Sódar, C. Soekmadji, J. Sotillo, P.D. Stahl, W. Stoorvogel, S.L. Stott, E.F. Strasser, S. Swift, H. Tahara, M. Tewari, K. Timms, S. Tiwari, R. Tixeira, M. Tkach, W.S. Toh, R. Tomasini, A.C. Torrecilhas, J.P. Tosar, V. Toxavidis, L. Urbanelli, P. Vader, B. W. van Balkom, S.G. van der Grein, J. Van Deun, M.J. van Herwijnen, K. Van Keuren-Jensen, G. van Niel, M.E. van Royen, A.J. van Wijnen, M.H. Vasconcelos, I. J. Vechetti, T.D. Veit, L.J. Vella, É. Velot, F.J. Verweij, B. Vestad, J.L. Viñas, T. Visnovitz, K.V. Vukman, J. Wahlgren, D.C. Watson, M.H. Wauben, A. Weaver, J. P. Webber, V. Weber, A.M. Wehman, D.J. Weiss, J.A. Welsh, S. Wendt, A. M. Wheelock, Z. Wiener, L. Witte, J. Wolfram, A. Xagorari, P. Xander, J. Xu, X. Yan, M. Yáñez-Mó, H. Yin, Y. Yuana, V. Zappulli, J. Zarubova, V. Žėkas, J. Zhang, Z. Zhao, L. Zheng, A.R. Zheutlin, A.M. Zickler, P. Zimmermann, A.M. Zivkovic, D. Zocco, E.K. Zuba-Surma, Minimal information for studies of extracellular vesicles 2018 (MISEV2018): a position statement of the International Society for Extracellular Vesicles and update of the MISEV2014 guidelines, J. Extracell. Vesicles 7 (2018) 1535750, https://doi.org/10.1080/20013078.2018.1535750.

[2] J.A. Welsh, et al., Minimal information for studies of extracellular vesicles (MISEV2023): From basic to advanced approaches, J. Extracell. Vesicles 13 (5) (2024) e12404, https://doi.org/10.1002/jev2.12451.

[3] R. Szatanek, M. Baj-Krzyworzeka, J. Zimoch, M. Lekka, M. Siedlar, J. Baran, The methods of choice for extracellular vesicles (EVs) characterization, Int. J. Mol. Sci. 18 (6) (2017) 1153, https://doi.org/10.3390/ijms18061153.

[4] P. Wu, B. Zhang, D.K.W. Ocansey, W. Xu, H. Qian, Extracellular vesicles: A bright star of nanomedicine, Biomaterials 269 (2021) 120467, https://doi.org/10.1016/j.biomaterials.2020.120467.

[5] K. Pachler, N. Ketterl, A. Desgeorges, Z. Dunai, S. Laner-Plamberger, D. Streif, D. Strunk, E. Rohde, M. Gimona, An in vitro potency assay for monitoring the immunomodulatory potential of stromal cell-derived extracellular vesicles, Int. J. Mol. Sci. 18 (7) (2017) 1413, https://doi.org/10.3390/ijms18071413.

[6] D. Di Silvestre, S. Garavelli, C. Procaccini, F. Prattichizzo, G. Passignani, V. De Rosa, P. Mauri, G. Matarese, P. de Candia, CD4+ T-Cell Activation Prompts Suppressive Function by Extracellular Vesicle-Associated MicroRNAs, Front. Cell. Dev. Biol. 9 (2021) 753884, https://doi.org/10.3389/fcell.2021.753884.

[7] M. Tkach, C. Théry, Communication by extracellular vesicles: where we are and where we need to go, Cell 164 (2016) 1226–1232, https://doi.org/10.1016/j.cell.2016.01.043.

[8] M. Manno, A. Bongiovanni, L. Margolis, P. Bergese, P. Arosio, The physico-chemical landscape of extracellular vesicles, Nat. Rev. Bioeng. 3 (1) (2025) 68–82, https://doi.org/10.1038/s44222-024-00255-5.

[9] L. Ripoll, A.M. Zickler, P. Vader, S. El Andaloussi, F.J. Verweij, G. van Niel, Biology and therapeutic potential of extracellular vesicle targeting and uptake, Nat. Rev. Mol. Cell. Biol. 27 (2026) 358–376, https://doi.org/10.1038/s41580-025-00922-4.

[10] B. Leonardini, M. Accorsi, R. Dimova, A. Relini, G. Rossi, E. Canepa, Understanding, mimicking, and exploiting lipid membrane fusion in biomedicine and synthetic biology, Adv. Phys. X 11 (1) (2026) 2636806, https://doi.org/10.1080/23746149.2026.2636806.

[11] J. van den Ende, K.A.Y. Defourny, H.H. Rabouw, M.E. Tanenbaum, R.W. Wubbolts, E.N.M. Nolte-'t Hoen, Development of a Live-Cell Imaging Assay to Elucidate Spatiotemporal Dynamics of Extracellular Vesicle Fusion with Target Cells, J. Extracell. Vesicles 15 (3) (2026) e70228, https://doi.org/10.1002/jev2.70228.

[12] R.R. Mizenko, V. Arun, D. Meshkanian, N.M. Lowe, H. Mohabbat, A. Wang, R. P. Carney, Single-particle characterization reveals heterogeneous extracellular vesicle fusion with liposomes, Small Methods 10 (2026) e01195, https://doi.org/10.1002/smtd.202501195.

[13] V. Rondelli, S. Helmy, G. Passignani, P. Parisse, D. Di Silvestre, Integrated strategies for a holistic view of extracellular vesicles, ACS Omega 7 (23) (2022) 19058–19069, https://doi.org/10.1021/acsomega.2c01003.

[14] F. Perissinotto, V. Rondelli, B. Senigagliesi, P. Brocca, L. Almásy, L. Bottyán, D. G. Merkel, H. Amenitsch, B. Sartori, K. Pachler, M. Mayr, M. Gimona, E. Rohde, L. Casalis, P. Parisse, Structural insights into fusion mechanisms of small extracellular vesicles with model plasma membranes, Nanoscale 13 (10) (2021) 5224–5233, https://doi.org/10.1039/d0nr09075a.

[15] C. Paba, V. Dorigo, B. Senigagliesi, N. Tormena, P. Parisse, K. Voitchovsky, L. Casalis, Lipid bilayer fluidity and degree of order regulates small EVs adsorption on model cell membrane, J. Colloid Interface Sci. 652 (2023) 1937–1943, https://doi.org/10.1016/j.jcis.2023.08.117.

[16] M. Grava, et al., Small extracellular vesicles impact on target membrane structure and dynamics, Il nuovo Cim. C. 45 (2022) 1–4, https://doi.org/10.1515/bmc-2022-0011.

[17] M. Grava, S. Helmy, M. Gimona, P. Parisse, L. Casalis, P. Brocca, V. Rondelli, Calorimetry of extracellular vesicles fusion to single phospholipid membrane, Biomol. Concepts 13 (2022) 148–155, https://doi.org/10.1515/bmc-2022-0011.

[18] L.A. Mulcahy, R.C. Pink, D.R.F. Carter, Routes and mechanisms of extracellular vesicle uptake, J. Extracell. Vesicles 3 (2014) 24641, https://doi.org/10.3402/jev.v3.24641.

[19] K.C. French, M.A. Antonyak, R.A. Cerione, Extracellular vesicle docking at the cellular port: Extracellular vesicle binding and uptake., in: *in Seminars in cell & developmental biology*, Elsevier, 2017, pp. 48–55, https://doi.org/10.1016/j.semcdb.2017.01.002.

[20] E. Chiricozzi, E. Di Biase, G. Lunghi, M. Fazzari, N. Loberto, M. Aureli, L. Mauri, S. Sonnino, Turning the spotlight on the oligosaccharide chain of GM1 ganglioside, Glycoconj. J. 38 (2021) 101–117, https://doi.org/10.1007/s10719-021-09974-y.

[21] H. Chahinian, N. Yahi, J. Fantini, Glutamate, gangliosides, and the synapse: electrostatics at work in the brain, Int. J. Mol. Sci. 25 (16) (2024) 8583, https://doi.org/10.3390/ijms25168583.

[22] M. Fazzari, G. Lunghi, E. Di Biase, M. Maggioni, E.V. Carsana, L. Cioccarelli, L. Vigani, N. Loberto, M. Aureli, L. Mauri, M.G. Ciampa, M. Valsecchi, K. Takato, A. Imamura, H. Ishida, O. Ben Mariem, S. Saporiti, L. Palazzolo, E. Chiricozzi, I. Eberini, S. Sonnino, GM1 structural requirements to mediate neuronal functions, Glycoconj. J. 40 (2023) 655–668, https://doi.org/10.1007/s10719-023-10141-8.

[23] Y. Fukuda, T. Fukui, C. Hikichi, T. Ishikawa, K. Murate, T. Adachi, H. Imai, K. Fukuhara, A. Ueda, A.P. Kaplan, T. Mutoh, Neurotropin promotes NGF signaling through interaction of GM1 ganglioside with Trk neurotrophin receptor in PC12 cells, Brain Res. 1596 (2015) 13–21, https://doi.org/10.1016/j.brainres.2014.11.041.

[24] R.W. Ledeen, G. Wu, The multi-tasked life of GM1 ganglioside, a true factotum of nature, Trends Biochem. Sci. 40 (2015) 407–418, https://doi.org/10.1016/j.tibs.2015.04.005.

[25] R.W. Ledeen, G. Wu, Gangliosides, α-Synuclein, and Parkinson's disease, Prog. Mol. Biol. Transl. Sci. 156 (2018) 435–454, https://doi.org/10.1016/bs.pmbts.2017.12.009.

[26] R. Ledeen, G. Wu, Gangliosides of the nervous system, Gangliosides Methods Protoc. (2018) 19–55, https://doi.org/10.1007/978-1-4939-8552-4_2.

[27] G. Lunghi, M. Fazzari, M.G. Ciampa, L. Mauri, E. Di Biase, E. Chiricozzi, S. Sonnino, Regulation of signal transduction by gangliosides in lipid rafts: focus on GM3–IR and GM1–TrkA interactions, FEBS Lett. 596 (2022) 3124–3132, https://doi.org/10.1002/1873-3468.14532.

[28] A. Varki, R.D. Cummings, M. Aebi, N.H. Packer, P.H. Seeberger, J.D. Esko, P. Stanley, G. Hart, A. Darvill, T. Kinoshita, J.J. Prestegard, R.L. Schnaar, H. H. Freeze, J.D. Marth, C.R. Bertozzi, M.E. Etzler, M. Frank, J.F. Vliegenthart, T. Lütteke, S. Perez, E. Bolton, P. Rudd, J. Paulson, M. Kanehisa, P. Toukach, K. F. Aoki-Kinoshita, A. Dell, H. Narimatsu, W. York, N. Taniguchi, S. Kornfeld, Symbol nomenclature for graphical representations of glycans, Glycobiology 25 (12) (2015) 1323–1324, https://doi.org/10.1093/glycob/cwv091.

[29] G. Lunghi, E. Di Biase, E.V. Carsana, A. Henriques, N. Callizot, L. Mauri, M. G. Ciampa, L. Mari, N. Loberto, M. Aureli, S. Sonnino, M. Spedding, E. Chiricozzi, M. Fazzari, GM1 ganglioside exerts protective effects against glutamate-excitotoxicity via its oligosaccharide in wild-type and amyotrophic lateral sclerosis motor neurons, FEBS Open. Bio 13 (12) (2023) 2324–2341, https://doi.org/10.1002/2211-5463.13727.

[30] M. Fazzari, E. Di Biase, L. Zaccagnini, A. Henriques, N. Callizot, M.G. Ciampa, L. Mauri, E.V. Carsana, N. Loberto, M. Aureli, L. Mari, M. Civera, F. Vasile, S. Sonnino, T. Bartels, E. Chiricozzi, G. Lunghi, GM1 oligosaccharide efficacy against α-synuclein aggregation and toxicity in vitro, Biochimica et Biophysica Acta (BBA)-Molecular Cell Biology Lipids 1868 (2023) 159350, https://doi.org/10.1016/j.bbalip.2023.159350.

[31] E. Di Biase, G. Lunghi, M. Maggioni, M. Fazzari, D.Y. Pomè, N. Loberto, M. G. Ciampa, P. Fato, L. Mauri, E. Sevin, F. Gosselet, S. Sonnino, E. Chiricozzi, GM1 oligosaccharide crosses the human blood–brain barrier in vitro by a paracellular route, Int. J. Mol. Sci. 21 (2020) 2858, https://doi.org/10.3390/ijms21082858.

[32] P.E.A. Rodríguez, G.N. Colmano, A. Pellegrini, M.E. Mariani, S.B. Rosso, G. Quassollo, P. Helguera, M. Bisbal, G.D. Fidelio, M.S. Sanchez, GM1-Oligosaccharide Rescues Rotenone-Impaired Neuronal Polarization Through RhoA/ROCK Modulation and Mitochondrial Protection, J. Neurochem. 170 (2026) e70505, https://doi.org/10.1111/jnc.70505.

[33] E. Chiricozzi, M. Maggioni, E. di Biase, G. Lunghi, M. Fazzari, N. Loberto, M. Elisa, F.G. Scalvini, G. Tedeschi, S. Sonnino, The neuroprotective role of the GM1 oligosaccharide, II3Neu5Ac-Gg4, in neuroblastoma cells, Mol. Neurobiol. 56 (10) (2019) 6673–6702, https://doi.org/10.1007/s12035-019-1556-8.

[34] S. Gurung, D. Perocheau, L. Touramanidou, J. Baruteau, The exosome journey: from biogenesis to uptake and intracellular signalling, Cell. Commun. Signal. 19 (1) (2021) 47, https://doi.org/10.1186/s12964-021-00730-1.

[35] O.V. Vieira, Rab3a and Rab10 are regulators of lysosome exocytosis and plasma membrane repair, Small GTPases 9 (2018) 349–351, https://doi.org/10.1080/21541248.2016.1235004.

[36] E. Di Biase, G. Lunghi, M. Fazzari, M. Maggioni, D.Y. Pomè, M. Valsecchi, M. Samarani, P. Fato, M.G. Ciampa, S. Prioni, L. Mauri, S. Sonnino, E. Chiricozzi, Gangliosides in the differentiation process of primary neurons: the specific role of GM1-oligosaccharide, Glycoconj. J. 37 (2020) 329–343, https://doi.org/10.1007/s10719-020-09919-x.

[37] G. Lunghi, M. Fazzari, E. Di Biase, L. Mauri, S. Sonnino, E. Chiricozzi, Modulation of calcium signaling depends on the oligosaccharide of GM1 in Neuro2a mouse neuroblastoma cells, Glycoconj. J. 37 (6) (2020) 713–727, https://doi.org/10.1007/s10719-020-09963-7.

[38] M. Fazzari, M. Audano, G. Lunghi, E. Di Biase, N. Loberto, L. Mauri, N. Mitro, S. Sonnino, E. Chiricozzi, The oligosaccharide portion of ganglioside GM1 regulates mitochondrial function in neuroblastoma cells, Glycoconj. J. 37 (2020) 293–306, https://doi.org/10.1007/s10719-020-09920-4.
[39] G. Tettamanti, F. Bonali, S. t Marchesini, V. Zambotti, A new procedure for the extraction, purification and fractionation of brain gangliosides, *Biochim. Et. Biophys. Acta (BBA)-Lipids Lipid Metab.* 296 (1973) 160–170, https://doi.org/10.1016/0005-2760(73)90055-6.
[40] D. Acquotti, L. Cantu, E. Ragg, S. Sonnino, Geometrical and conformational properties of ganglioside GalNAc-GD1a, IV4GalNAcIV3Neu5AcII3Neu5AcGgOse4Cer, Eur. J. Biochem. 225 (1994) 271–288, https://doi.org/10.1111/j.1432-1033.1994.00271.x.
[41] E. Chiricozzi, L. Mauri, G. Lunghi, E. Di Biase, M. Fazzari, M. Maggioni, M. Valsecchi, S. Prioni, N. Loberto, D.Y. Pomè, M.G. Ciampa, P. Fato, G. Verlengia, S. Cattaneo, R. Assini, G. Wu, S. Alselehdar, R.W. Ledeen, S. Sonnino, Parkinson's disease recovery by GM1 oligosaccharide treatment in the B4galnt1+/− mouse model, Sci. Rep. 9 (2019) 19330, https://doi.org/10.1038/s41598-019-55885-2.
[42] E. Chiricozzi, E.D. Biase, M. Maggioni, G. Lunghi, M. Fazzari, D.Y. Pomè, R. Casellato, N. Loberto, L. Mauri, S. Sonnino, GM 1 promotes TrkA-mediated neuroblastoma cell differentiation by occupying a plasma membrane domain different from TrkA, J. Neurochem. 149 (2019) 231–241, https://doi.org/10.1111/jnc.14685.
[43] E. Chiricozzi, D.Y. Pomè, M. Maggioni, E. Di Biase, C. Parravicini, L. Palazzolo, N. Loberto, I. Eberini, S. Sonnino, Role of the GM 1 ganglioside oligosaccharide portion in the TrkA-dependent neurite sprouting in neuroblastoma cells, J. Neurochem. 143 (2017) 645–659, https://doi.org/10.1111/jnc.14146.
[44] F. St-Denis-Bissonnette, H. Halabi, M. Creskey, M. Kirkby, X. Zhang, D. Burger, L. Wang, J.R. Lavoie, Ultracentrifugation and Ultrafiltration Differentially Alter the Composition and Functionality of the Biomolecular Corona of Extracellular Vesicles, J. Extracell. Biol. 5 (4) (2026) e70132, https://doi.org/10.1002/jex2.70132.
[45] S. Helmy, P. Brocca, A. Koutsioubas, S.C. Hall, L. Puricelli, P. Parisse, L. Casalis, V. Rondelli, A supported lipid bilayer to model solid-ordered membrane domains, J. Colloid Interface Sci. 690 (2025) 137333, https://doi.org/10.1016/j.jcis.2025.137333.
[46] V. Rondelli, P. Brocca, N. Tranquilli, G. Fragneto, E. Del Favero, L. Cantù, Building a biomimetic membrane for neutron reflectivity investigation: Complexity, asymmetry and contrast, Biophys. Chem. 229 (2017) 135–141, https://doi.org/10.1016/j.bpc.2017.04.011.
[47] P. Lago, L. Rovati, L. Cantó, M. Corti, A quasielastic light scattering detector for chromatographic analysis, Rev. Sci. Instrum. 64 (1993) 1797–1802, https://doi.org/10.1063/1.1144013.
[48] J. Stetefeld, S.A. McKenna, T.R. Patel, Dynamic light scattering: a practical guide and applications in biomedical sciences, Biophys. Rev. 8 (2016) 409–427, https://doi.org/10.1007/s12551-016-0218-6.
[49] D. Nečas, P. Klapetek, Gwyddion: an open-source software for SPM data analysis, Cent. Eur. J. Phys. 10 (2012) 181–188, https://doi.org/10.2478/s11534-011-0096-2.
[50] M. Doucet, et al., SasView version 5.0. 4, Zenodo (2020).
[51] L. Almásy, New measurement control software on the Yellow Submarine SANS instrument at the Budapest Neutron Centre, J. Surf. Investig. X-ray Synchrotron Neutron. Tech. 15 (2021) 527–531, https://doi.org/10.1134/S1027451021030046.
[52] C. Balbi, P. Parisse, H. Vondracek, E. Lazzarini, S. Bolis, T.E. Fertig, M. Gherghiceanu, L. Barile, G. Vassalli, Impact of isolation methods on extracellular vesicle functionality in vitro and in vivo, Adv. Biol. 8 (2024) 2300185, https://doi.org/10.1002/adbi.202300185.
[53] G. Birarda, D. Bedolla, F. Piccirilli, C. Stani, H. Vondracek, L. Vaccari, Z. Huang, Chemical analyses at micro and nano scale at SISSI-Bio beamline at Elettra-Sincrotrone Trieste, in: in Biomedical Vibrational Spectroscopy 2022: Advances in Research and Industry, SPIE, 2022, pp. 27–39, https://doi.org/10.1117/12.2607751.
[54] J. Demšar, et al., Orange: data mining toolbox in Python, J. Mach. Learn. Res. 14 (2013) 2349–2353. https://www.jmlr.org/papers/volume14/demsar13a/demsar13a.pdf.
[55] J. Mihály, R. Deák, I.C. Szigyártó, A. Bóta, T. Beke-Somfai, Z. Varga, Characterization of extracellular vesicles by IR spectroscopy: Fast and simple classification based on amide and CH stretching vibrations, Biochim. Et. Biophys. Acta (BBA)-Biomembr. 1859 (3) (2017) 459–466, https://doi.org/10.1016/j.bbamem.2016.12.005.
[56] A. Koutsioubas, anaklasis: a compact software package for model-based analysis of specular neutron and X-ray reflectometry data sets, Appl. Crystallogr. 54 (2021) 1857–1866, https://doi.org/10.1107/S1600576721009262.
[57] G. Salvetti, C. Cardelli, C. Ferrari, E. Tombari, A modulated adiabatic scanning calorimeter (MASC), Thermochim. Acta 364 (2000) 11–22, https://doi.org/10.1016/S0040-6031(00)00645-6.
[58] K. Zycienska, K. Życieńska, B. Pszczółkowska, B. Brzozowska, M. Kamiński, T. Lorenc, W. Olejarz, S. Sęk, J. Ginter, Brownian Motion Influence on AFM Exosomes' Size Measurements, Int. J. Mol. Sci. 23 (17) (2022) 10074, https://doi.org/10.3390/ijms231710074.
[59] Z. Varga, Y. Yuana, A.E. Grootemaat, E. van der Pol, C. Gollwitzer, M. Krumrey, R. Nieuwland, Towards traceable size determination of extracellular vesicles, J. Extracell. Vesicles 3 (1) (2014) 23298, https://doi.org/10.3402/jev.v3.23298.
[60] R. Di Santo, S. Romanò, A. Mazzini, S. Jovanović, G. Nocca, G. Campi, M. Papi, M. De Spirito, F. Di Giacinto, G. Ciasca, Recent advances in the label-free characterization of exosomes for cancer liquid biopsy: from scattering and spectroscopy to nanoindentation and nanodevices, Nanomaterials 11 (2021) 1476, https://doi.org/10.3390/nano11061476.
[61] A. Accardo, L. Tirinato, D. Altamura, T. Sibillano, C. Giannini, C. Riekel, E. Di Fabrizio, Superhydrophobic surfaces allow probing of exosome self organization using X-ray scattering, Nanoscale 5 (6) (2013) 2295–2299, https://doi.org/10.1039/c3nr34032e.
[62] A. Ridolfi, M. Brucale, C. Montis, L. Caselli, L. Paolini, A. Borup, A.T. Boysen, F. Loria, M.J.C. van Herwijnen, M. Kleinjan, P. Nejsum, N. Zarovni, M.H. M. Wauben, D. Berti, P. Bergese, F. Valle, AFM-based high-throughput nanomechanical screening of single extracellular vesicles, Anal. Chem. 92 (15) (2020) 10274–10282, https://doi.org/10.1021/acs.analchem.9b05716.
[63] E. Mahieu, F. Gabel, Biological small-angle neutron scattering: recent results and development, Biol. Crystallogr. 74 (8) (2018) 715–726, https://doi.org/10.1107/s2059798318005016.
[64] D. Lingwood, K. Simons, Lipid rafts as a membrane-organizing principle, Science (1979) 327 (5961) (2010) 46–50, https://doi.org/10.1126/science.1174621.
[65] M.L. Kraft, Sphingolipid organization in the plasma membrane and the mechanisms that influence it, Front. Cell. Dev. Biol. 4 (2017) 154, https://doi.org/10.3389/fcell.2016.00154.
[66] L.J. Pike, The challenge of lipid rafts, J. Lipid Res. 50 (2009) S323–S328, https://doi.org/10.1194/jlr.R800040-JLR200.
[67] T. Róg, I. Vattulainen, Cholesterol, sphingolipids, and glycolipids: what do we know about their role in raft-like membranes? Chem. Phys. Lipids 184 (2014) 82–104, https://doi.org/10.1016/j.chemphyslip.2014.10.004.
[68] G. van Meer, Dynamic transbilayer lipid asymmetry, Cold Spring Harb. Perspect. Biol. 3 (5) (2011), https://doi.org/10.1101/cshperspect.a004671 a004671-a004671.
[69] J. Cardellini, A. Ridolfi, M. Donati, V. Giampietro, M. Severi, M. Brucale, F. Valle, P. Bergese, C. Montis, L. Caselli, D. Berti, Probing the coverage of nanoparticles by biomimetic membranes through nanoplasmonics, J. Colloid Interface Sci. 640 (2023) 100–109, https://doi.org/10.1016/j.jcis.2023.02.073.
[70] J. Peters, J. Marion, F.J. Becher, M. Trapp, T. Gutberlet, D.J. Bicout, T. Heimburg, Thermodynamics of lipid multi-lamellar vesicles in presence of sterols at high hydrostatic pressure, Sci. Rep. 7 (2017) 15339, https://doi.org/10.1038/s41598-017-15582-4.
[71] N.M.E. Ayad, S. Kaushik, V.M. Weaver, Tissue mechanics, an important regulator of development and disease, Philos. Trans. R. Soc. B 374 (1779) (2019) 20180215, https://doi.org/10.1098/rstb.2018.0215.